Optical Wireless Communications: new opportunities and applications

by Alessandro Sturniolo

Sant'Anna
School of Advanced Studies – Pisa

Academic Year
2017/2018
Phd Course in
Emerging Digital
Technologies

Optical Wireless Communications: new opportunities and applications

Author
Alessandro Sturniolo

Supervisor
Ernesto Ciaramella

Tutor
Giulio Cossu

Contents

Acronyms

AC Alternating Current

ADC Analog-to-Digital Converter

APD Avalanche Photodiode

AR Augmented Reality

ARM/FPGA FPGA-based Application Real-time Microcontroller board

ASK Amplitude Shift Keying

AUV Autonomous Underwater Vehicle

AWGN Additive Gaussian White Noise

BER Bit Error Ratio

BG Background

BJPR Beacon Jointed Packet Reconstruction

CCD Charge-Coupled Device

CCT Correlated Color Temperature

CDR Clock and Data Recovery

CDS Correlated Double Sampler

CIS Camera Image Sensor

CMOS Complementary Metal Oxide Semiconductor

CSK Color Shift Keying

DC Direct Current

DD Displacement Damage

DFB Distributed FeedBack

D-LOS Directed Line-of-Sight

DMT Discrete Multi-Tone

D-NLOS Directed Non-Line-of-Sight

DSP Digital Signal Processing

E.M. electromagnetic

EMI Electro-Magnetic Interference

FFT Fast Fourier Transform

FOV Field-of-View

FPGA Field-Programmable Gate Array

FTU Formazin Turbidity Unit

fps frames per second

GaN Gallium Nitride

GS Global Shutter

HEP High-Energy Physics

HetNet Heterogeneous Networks

HT-DLOS High Tolerance DLOS

IM/DD Intensity Modulation with Direct Detection

IoT Internet of Things

IPS Indoor Positioning System

IR Infrared

IrDA InfraRed Data Association

LAN Local Area Network

LASER Light Amplification by Stimulated Emission of Radiation

LD Laser Diode

LED Light Emitting Diode

LOON Littoral Ocean Observatory Network

LOS Line-of-Sight

MIMO Multiple Input Multiple Output

mm-wave Millimeter-Wave

MOS Metal Oxide Semiconductors

ND-LOS Non-Directed Line-of-Sight

ND-NLOS Non-Directed Non-Line-of-Sight

NRZ Non-Return to Zero

OCC Optical Camera Communication

OLED Organic Light Emitting Diode

OOK On-Off Keying

OSNR Optical Signal-to-Noise Ratio

OWC Optical Wireless Communication

PAN Personal Area Network

Ph-LED Phosphor LED

PIN Positive-Intrinsic-Negative

PD photodiode

PRBS Pseudo Random Bit Sequence

PSD Power Spectral Density

RF Radio Frequency

RMS Root-Mean-Square

RoI Region of Interest

ROV Remotely Operated Vehicle

RS Rolling Shutter

RX receiver

RZ Return to Zero

SDCS Software Defined Communication Stack

SNR Signal-to-Noise Ratio

TIA Trans-Impedance Amplifier

TX transmitter

UAV Unmanned Autonomous Vehicle

UOWC Underwater Optical Wireless Communication

UWSN Underwater Wireless Sensor Network

VCSEL Vertical Cavity Surface Emitting LASER

VLC Visible Light Communication

VLCA Visible Light Communication Association

VLCC Visible Light Communications Consortium

VPN Virtual Private Network

WDM Wavelength Division Multiplexing

YAG Yttrium Aluminum Garnet

Abstract

Optical Wireless Communications (OWCs) are a family of technologies for wireless communications which exploit optical signals for data transmission. More generally the term OWC is used to describe an optical communication in the near-Infrared (IR) portion of the electromagnetic spectrum, while transmissions in the visible range ($380 - 780\ nm$) are usually referred to as Visible Light Communications (VLCs).
The first papers about OWC can be traced back to the '70s [1], and to 2001 for VLC. InfraRed Data Association (IrDA), founded in 1993, provided the standardization for IR communications to push the commercial development of this technology. On the other side, it was necessary to wait until 2003 for visible technology to become subject of interest outside the academic world with the founding of the Visible Light Communications Consortium (VLCC) in Japan , that in 2014 became Visible Light Communication Association (VLCA) [2]. Although a vast segment of these writings is represented by telecommunications, there are relevant contributions, new concepts and ideas, that branched to address novel applications and features.
Moreover, the evolution of the Internet of Things (IoT) and of the "always connected" paradigm has highlighted the limitations of widespread wireless radio systems. Interference, strictly regulated bandwidth and environmental constrains represent obstacles that affect Radio Frequency (RF) signals and hence limit the development of RF-based applications.
Among these, secure Personal Area Network (PAN), underwater communications for autonomous vehicles or transmission systems for high radiation environments represent a range of applications that can be addressed by OWC technology.
This thesis addresses the study and the design of OWC and VLC systems as an alternative to RF communications, in particular whenever RF are not suitable for specific applications. The thesis is organized as follows:
Chapter 1 details the known limits and issues of RF systems and a brief

description of the OWC and VLC alternatives already explored for selected applications.
Chapter 2 presents a general description of OWC communications, describing their general features, adopted devices, channel properties and modulation formats.
Chapter 3 describes the design and testing of a VLC prototype embedded in a common table lamp for indoor PAN with an extended characterization of its performances.
Chapter 4 reports the design and testing of a Optical Camera Communication (OCC) system with a novel approach to the use of Region of Interest (RoI) algorithms to improve signal processing and reduce channel losses.
Chapter 5 relates to the design, realization and testing of a pair of underwater optical modems that provide Ethernet connection in harsh conditions in an operative scenario.
Chapter 6 finally summarizes the contributions presented in the previous chapters and gives a picture of the future possible developments of the applications explored in this thesis.

Acknoledgements

I would like to express my gratitude to professor Ernesto Ciaramella for his guidance and help along this three years that shaped me on a human and professional level.
I must highlight here that all the achievements of this thesis would not have been possible without Dr. Giulio Cossu. He mentored me in this journey and never refused to spend an helping word, whichever the situation.
During my PhD I had the privilege to be hosted as visiting researcher at Northumbria University in Newcastle upon Tyne, UK. It was an incredible opportunity to be there and an absolute pleasure. I shared ideas and beautiful moments with professor Zabih Ghassemlooy and all the colleagues and friends of Newcastle: Navid, Andrew, Khald, Osama and Hubert.
Thanks to all the friends that I found here in Pisa and built my new life outside of my hometown: thanks to Mario, Antonella, Stella, Silvia e Fabio.
To the friends that chose to come here from my hometown to follow my same path, helping me with my "Romesickness": thanks to Alessandro, Lorenzo and Federico.
I owe deep gratitude to my Buddhist community and my mentor Daisaku Ikeda for their constant support and encouragement.
I would like to state all my gratefulness for my family: my father, my mother and my grandmother. Although it required a fair share of hard work and effort to reach this point, I must admit that it was easy to touch the clouds by standing on the shoulders of giants.
Finally my greatest thanks goes to Sara, the person that have shared my everyday wins and losses, my happiness and my deep sorrows. Thanks for being with me and to be yourself and nothing less in every single day of our life together.
I love you.

Chapter 1

New frontiers of communications

New technology trends and the sustained growth of mobile communications are stretching the limits of the widely adopted Radio Frequency (RF) wireless technology. People working in Optical Wireless Communication (OWC) explored since the '70s the use of optical signals as an alternative [1]. A typical OWC uses an optical source, like a Light Emitting Diode (LED) or a Light Amplification by Stimulated Emission of Radiation (LASER) device, as transmitter. By modulating the emitted optical power and using a photodetector to translate the optical signal into the electrical domain is possible to convey an information at a certain distance.
The development of high brightness and efficient visible LEDs for lighting infrastructures represents one of the main factors that allowed the creation of Visible Light Communication (VLC).
Nowaday, lighting accounts for up to 15% of the global electricity consumption and up to 5% of world greenhouse emissions [3]. Common LED lamps today use 85% less energy than incandescence-based lightbulbs and their diffusion has already showed a positive impact on energy consumption that will grow in future. Moreover, following the improvements in manufacturing and devices' electronics, LED cost has substantially dropped in the last years [4].
Compared to traditional lighting devices (incandescence lightbulbs, fluorescent tubes, halogen lamps etc.), LED lamps can benefit from a wider modulation band due to a faster response to electric current variations. This feature can be exploited to deploy new services by means of lighting infrastructures as novel medium for data network, achieving bit rates higher than

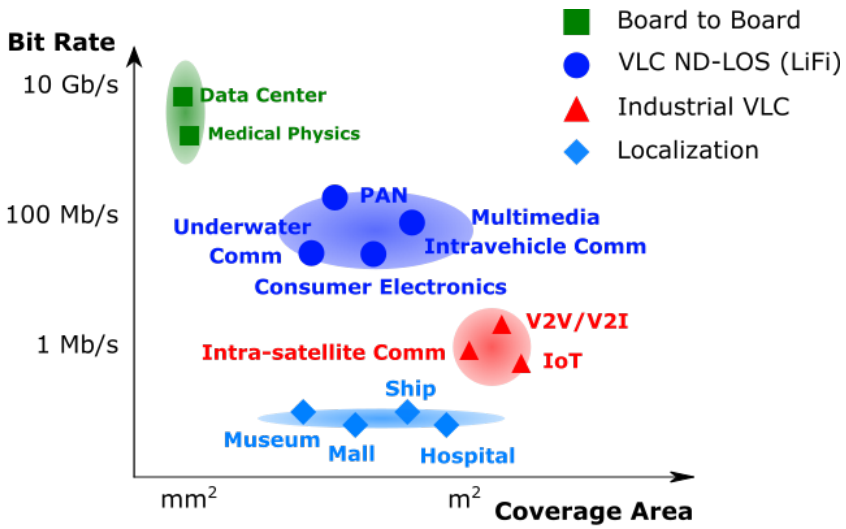

Figure 1.1: The different characteristics and performance of the novel OWC and VLC systems are paving the road for new wireless scenarios.

Wi-Fi systems (see Fig. 1.1).

1.1 Limits and issues of radio systems

In the last century, wireless radio communications, which are now pervasive, changed the life of citizens by various technological implementations, such as radio, TV, satellite, cellular, Bluetooth and Wi-Fi, as summarized in Fig. 1.2.

RF waves have strong potential in wireless communications: thanks to diffraction, the corresponding signals can cover wide areas and are robust to shadowing. However, the same physical features of RF wireless communications that represent a unique advantage prevent their use in various wireless applications:

- are prone to interference phenomena limiting their use in sensible application scenarios (e.g. hospitals, high-security environments) or to jamming by external attackers;
- can be affected by the presence of high radiations or strong electro-

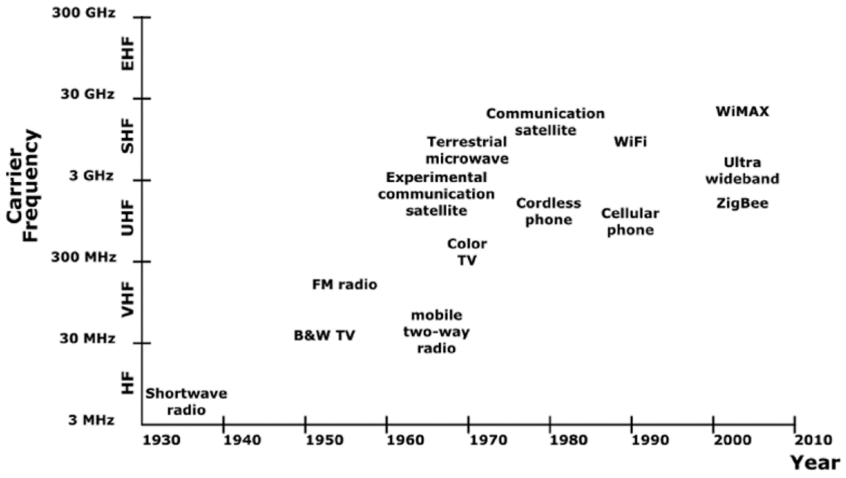

Figure 1.2: RF wireless applications presented with their frequency band and developing year

magnetic fields;

- due to strong attenuation in water are limited to very short transmission distances ($<< 1\ m$);
- long propagation radius, multipath and fading effects limit the density of wireless nodes that can be deployed and hence limit the user density.
- propagation distance and robustness to shadowing also imply an easy access to transmitted information, that can be intercepted by unwanted eavesdroppers.
- as the maximum bit rate achievable is a function of the maximum frequency available, reaching very high bit rate (e.g. 10 $Gbit/s$) is very hard using RF signals; these issues are partially accounted when higher carrier frequency is considered (e.g. 60 GHz), but this means approaching the domain of conventional optics, i.e. moving to the region where diffraction effects become lower and lower.

The issues related to the scarcity of resources available have their roots in the limits and rules that govern the RF spectrum allocation. The entire RF spectrum spans a range of approximately 300 GHz, with most part of it being licensed or subject to limitations (see Fig. 1.3). Instead, the visible light alone stretches from approximately 430 THz to 770 THz, giving an

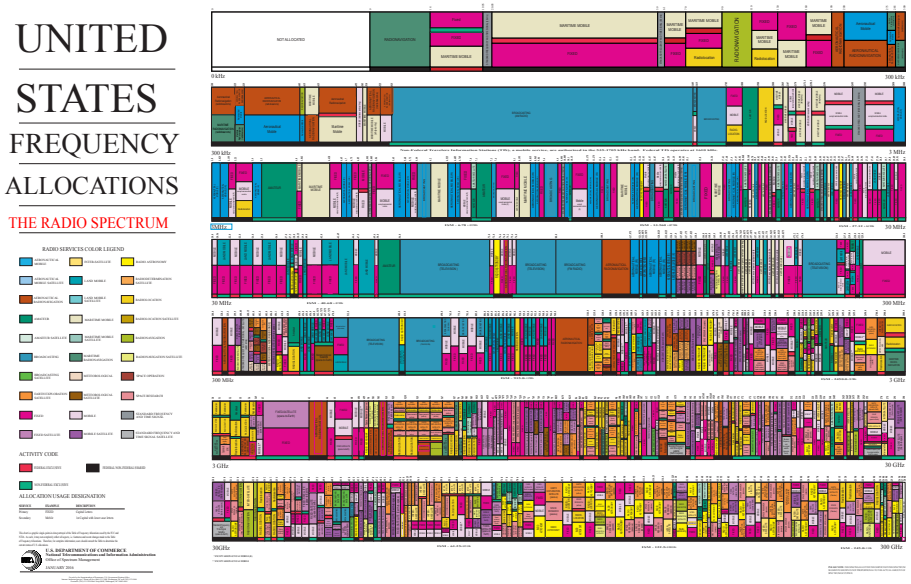

Figure 1.3: US RF spectrum allocation [5]

unlicensed spectrum roughly 1000 times bigger than RF.

Since the '50s, wireless networks improved their capacity by a factor 10^6, redoubling the available data rate approximately every 30 months, as predicted by Cooper's Law [6].

According to Cisco Visual Networking Index [7], mobile communications demand is expected to grow at a rate of more than 50% per year. With the advent of the Internet of Things (IoT), the number of devices connected to the global network will reach 20 billion in 2020. The general trend can be already observed with the milestone reached in 2017, of more object (8.35 billion) connected than human beings alive (7.5 billions) [8].

As shown in Fig. 1.4, more than 60% of all wireless data were sent through Wi-Fi in 2017. Both reported and predicted demand of mobile traffic highlight the growing of the unmet demand due to shortage of wireless capacity through the years.

In order to increase the capacity of wireless radio systems there are three ways:

- Obtain more bandwidth by releasing new spectrum
- Enhance the spectral efficiency

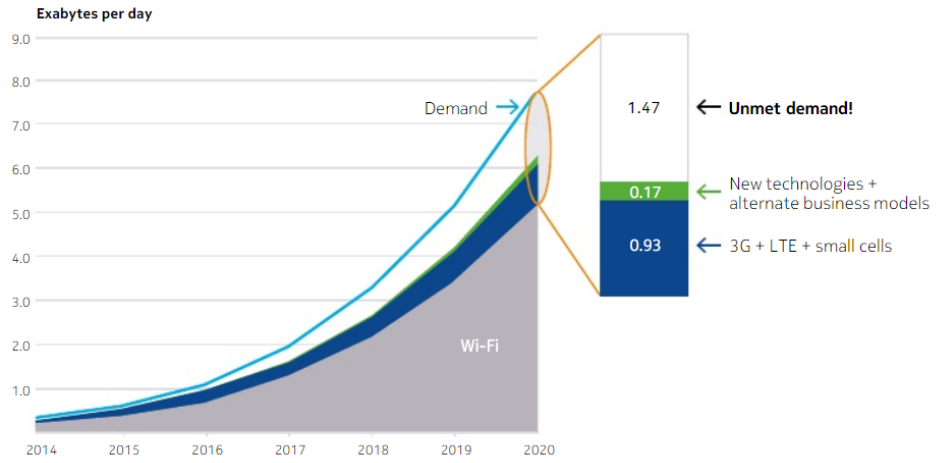

Figure 1.4: Demand for wireless data traffic recorded and forecast [9]

- Multiply the availability of nodes

The complexity of the first solution can be deducted by the picture presented in Fig. 1.3, portraying the current frequency allocation in the USA, which clearly represent the ongoing congestion of the RF spectrum. For example WiGig technology, defined by IEEE 802.11ad and IEEE 802.11ay, operate in the 60 GHz spectrum, taking advantage of 14 GHz of spectrum shared with other applications. In order to achieve the required performance, WiGig and other Millimeter-Wave (mm-wave) technologies require solutions like beam-forming, using multiple antennas and individual phase shifters. These devices can highly increase hardware complexity, power consumption and costs.
About increasing the efficiency of spectrum usage, in the last 25 years it has accounted only for a minor improvement of the capacity [10] that cannot solve the foreseen request of new resources.
Node multiplication in mobile networks is usually achieved by splitting existing cells, e.g. Heterogeneous Networks (HetNet). This process adds complexity to the network management due to an exponential growth in node-to-node handover of moving devices. Moreover, the interference between nodes need to be addressed, reducing the available bandwidth, i.e. dividing a cell in two different nodes do not duplicate its capacity.

1.2 New opportunities and applications

The previous section exposed the problems that affect wireless RF systems, highlighting various application that are not suitable for their implementation. While taking advantage of many of the improvements of radio communications, VLC shows substantial differences due to the very nature of the carrier: the visible light. These features have paved the road for novel wireless applications and higher bit rates.

High-speed wireless data transmissions

The availability of a wider spectrum and of a higher carrier frequency contribute to the realization of high-speed wireless systems ($> 10\ Gbit/s$ bit rate) that are not possible with RF signals. This opens the way to wireless links for data centers and other high-demanding applications.

Personal Area Networks (PAN)

The advent of IoT brought a great variety of devices for communication assistance, entertainment, fitness and medical monitoring. These "wearable" devices currently operate by means of RF systems, such as Bluetooth or ZigBee, building up what is called a Personal Area Network (PAN). While their application needs only $1-2\ m$ range, both Bluetooth and ZigBee transmit up to $10\ m$, exposing the user to dangerous intrusions and data losses. Compared to RF emissions, light is absorbed by optically opaque obstacles and, due to its shorter wavelength ($0.3 - 1.6\ \mu m$), is not diffracted or scattered by macroscopic objects ($> 1\ mm$). These characteristics account for a natural confinement of optical signals in close environments that result for an embedded security level at the physical layer.

Underwater Optical Wireless

The use of RF electromagnetic waves has pushed the exploration and exploitation of air and space, allowing for fast and reliable communications even at very long distance. Surprisingly, it is estimated that only the 5% of the world's oceans and 1% of the oceans floor has been explored [11]. The reason for this is that water represents a heavy absorbing medium for RF electromagnetic waves, limiting their use for near surface applications and forcing the use of low bit rate (< 40 kb/s) acoustic systems for underwater transmissions [12]. Sea-water has a low-loss window in the visible region that

can be conveniently exploited by Underwater Optical Wireless Communications (UOWCs). Thanks to this, UOWCs can offer much higher bit-rates, compared to acoustic modems, although at shorter distances. Combining high-speed and wireless transmission, the UOWCs represent a valid alternative, which is rapidly gaining popularity for deployment on Unmanned Autonomous Vehicles (UAVs), Remotely Operated Vehicles (ROVs) and Underwater Wireless Sensor Networks (UWSNs).

Communications in high-radiation environment

Strong ionizing radiations represent not only a source of potential harm to biological tissues but can also impair communication systems. Either by ionization or Displacement Damage (DD), radiation can damage or hamper the performance of devices and wiring, reducing their lifetime in a consistent way. By reducing the amount of exposed matter, wireless systems provide a favourable solutions to this issue. However, often high-radiation environments are related to high levels of Electro-Magnetic Interference (EMI) that can hinder RF communications. Being immune to EMI, OWC systems can overcome this limit, offering a viable solution for high-radiation applications, e.g. High-Energy Physics (HEP) experiments detectors or intra-satellite and inter-satellite communications.

Optical Camera Communications

VLC that use digital optical cameras as receiver (RX) instead of photodiodes (PDs) are called Optical Camera Communications (OCCs).
Digital camera sensors can be generally described as a compact array of PDs this offers unique features for a VLC system:

- spatial and color domains separation of multiple transmitter (TX) not possible with a single PD-based RX [13];
- large field of view;
- low bit rate transmissions with non-flickering illumination using low frame-rate cameras [14].

However, OCC-based VLC links, are affected by issues related to ambient noise, low data rates and mobility [15]. In OCC, the limited number of frames per second (fps) at the RX represent one of the main limitations in data transmission.

Nonetheless, due to the pervasive presence of digital camera in consumer electronics, OCC technology represent today the strongest candidate for the initial deploy of VLC systems.
Among the possible applications of OCCs there are Indoor Positioning System (IPS), integration in IoT systems, smart cities and Augmented Reality (AR) systems, e.g. to transmit information to visitors in expositions or to dispatch evacuation direction in close environments.

Chapter 2

Optical Wireless Communication Systems

A communication system conveys information from a source to a destination positioned at a certain distance. This system is characterized by a set of building blocks, as portrayed in Fig. 2.1:

1. The source of information, generates the data to be transmitted;
2. The modulator, which converts the logical data into a physical signal (e.g. electrical signal);
3. The transmitter, translating the modulated signal into a form suitable for the transmission medium (channel);
4. The channel, which links the source to the destination;
5. The receiver, to recover the translated signal from the channel;
6. The demodulator, to extract again the information from the signal;

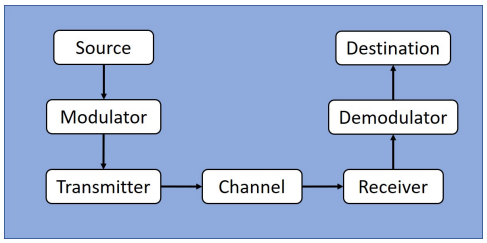

Figure 2.1: Building block scheme for a generalized communication system.

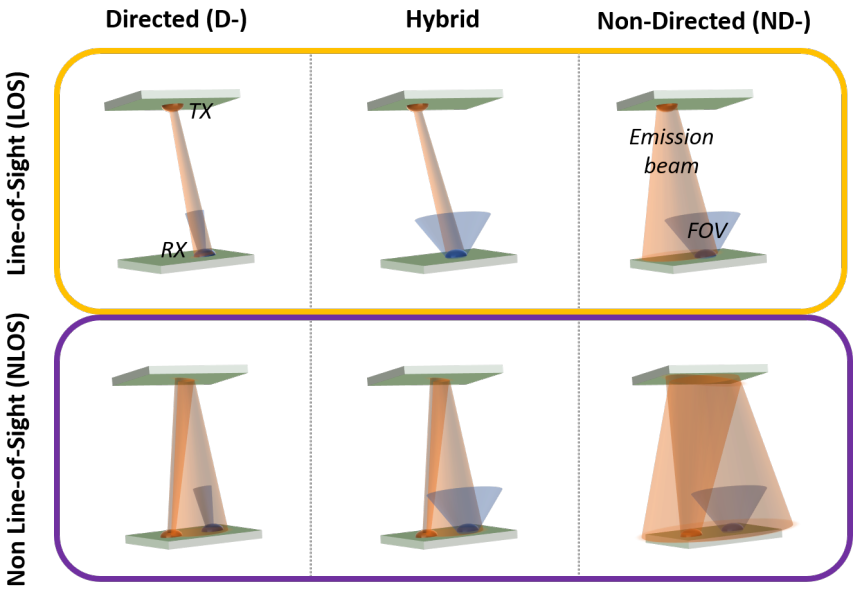

Figure 2.2: OWC links possible configuration. TX is the transmitter, RX is the receiver and FOV is the Field-of-View.

7. The destination, which is the final target of the information.

In this chapter, we will focus on the building blocks that are necessary to the realization of a communication system, describing how this general scheme applies to the optical wireless case.
A more detailed description of the specific OWC applications will be presented in the next chapters.

2.1 System configurations

Link geometry deeply influences OWC systems performance and the device choice. Based on TX/RX Field-of-View (FOV) and link directionality, we can define 6 different configurations (see Fig. 2.2). Related to FOV, links can be defined as Directed (D-) or Non-Directed (ND-). Link directionality can be defined Line-of-Sight (-LOS) for a direct communication between TX and RX or as Non-Line-of-Sight (-NLOS) if the optical link is maintained through a reflected or diffused beam.

- In **Directed Line-of-Sight (D-LOS)** (see Fig. 2.2, top left) TX and RX are directed along the same optical axis in two opposing directions

with no obstacles in between. The communication channel is compressed in a narrow beam by using a small angle emitter at TX side and a narrow FOV at RX side. This configuration is usually adopted for point-to-point topology. In terms of optical power, this geometry is the lowest power-demanding due to the high confinement of the signal in a narrow beam and hence a high power density, a reduced noise from ambient light and multipath-induced signal distortion at the RX side. However this configuration requires a careful alignment of TX and RX reducing the link mobility or requiring a tracking system. Moreover, the breaking of the LOS by intervening objects (shadowing) disrupts the communication, heavily limiting the use of this configuration in many environments.

- In order to increase the link robustness to misalignment and shadowing, **Non-Directed Line-of-Sight (ND-LOS)** configuration (top right) represents a valid alternative to implement point-to-multipoint and broadcast topologies. In ND-LOS systems, using a wider emission angle and a wider RX FOV, the need for TX-RX careful alignment is usually removed, allowing for devices mobility. However, link robustness is improved at the expenses of power efficiency, background noise and multipath dispersion rejection, affecting overall link performance.

- A trade-off between these configurations is represented by the **hybrid Line-of-Sight (LOS)** configuration (top central), which uses either narrow TX emission angle or RX FOV. In particular in **High Tolerance DLOS (HT-DLOS)**, a larger emission angle and a narrow RX FOV can be used to achieve high communication performance while providing robustness to misalignment, useful to realize a point-to-point topology requiring just a coarse alignment. The opposite situation can be used in multipoint-to-point or star topologies.

- **Directed Non-Line-of-Sight (D-NLOS)** systems (bottom left), due to use of reflected paths are more robust to both shadowing and misalignment than D-LOS systems, although having lower performances. However, the use of direct configuration still poses a major constrain to mobility related to the need for alignment, even if not so accurate.

- **Non-Directed Non-Line-of-Sight (ND-NLOS)** configuration, also defined as **diffused**, is the most robust configuration (bottom right) regarding both alignment and shadowing, due to the use of wide emis-

sion TXs and wide FOV RXs. It is obvious that the high optical path loss and multipath dispersion, together with a higher degree of background noise, greatly reduces the performance of diffused systems. Still, this configuration is considered the more versatile in terms of achievable topologies and applications.

- **Hybrid NLOS** configuration (bottom central), like their LOS counterparts, represents trade-offs between direct and non-direct performances and robustness, leveraging different TX emission angle and RX FOV.

2.2 Transmitting devices

A typical optical TX employs a semiconductor diode that emits light. When this diode is forward biased, electrons flow in the semiconductor, recombining with the holes within. Electron-hole recombination generates photons by electroluminescence effect, with an energy, and hence a wavelength, dependent on the semiconductor band-gap. The optical emission can be spontaneous, as in LEDs and Organic Light Emitting Diodes (OLEDs), or stimulated, as in lasers, like Laser Diodes (LDs), Distributed FeedBack (DFB) lasers and Vertical Cavity Surface Emitting LASERs (VCSELs).
This thesis will deal only with OWCs based on LEDs. In what follows we will then focus our attention only on this type of sources.

2.2.1 Electrical characteristics of diodes

From an electrical point of view, diodes are non-linear devices, with an I-V characteristic (see Fig. 2.3) that obeys to the Shockley equation [16]

$$I_d = I_0[exp(qV_d/\eta k_B T) - 1] \tag{2.2.1}$$

where k_B is the Boltzmann constant, q is the electron charge, T is the junction temperature, η is the diode ideality factor that depends on the semiconductor, V_d is the junction voltage and I_0 represents the device leakage current when biased in the reverse direction ($V_d < 0$).
From the I-V characteristic (see Fig. 2.3) it can be easily seen that diodes are non-linear devices. Hence, the use of high-amplitude signals may cause distortions due to clipping effects. By keeping the device in the small signal regime is possible to avoid non-linear effects that appear at higher voltages. In small signals regime, diodes can be modeled as the forward biased ($V_d > 0$) equivalent circuit showed in Fig. 2.4, where r_s is the diode series resistance,

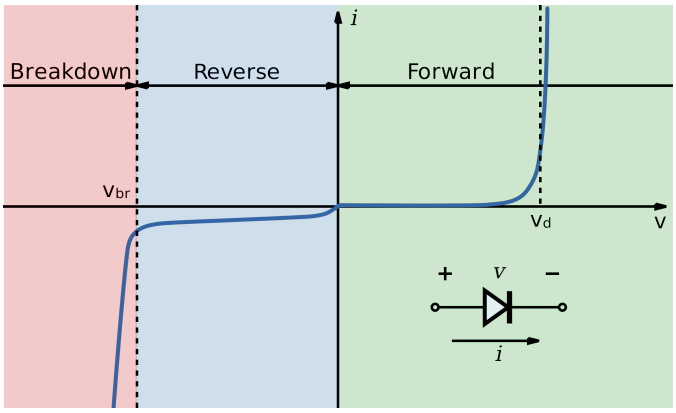

Figure 2.3: I-V characteristic of a semiconductor diode: V_{br} is the device breakdown voltage, V_d is the diode voltage knee. Three colored areas represent the three diodes regimes.

r_d is the diode small signals resistance.

The diode intrinsic capacitance is modeled as the sum of the junction capacitance

$$C_j = \left| \frac{dQ_j}{dV} \right|,$$

related to the variation of the total depletion-layer charge Q_j at the P-N interface as a function of the applied voltage V, and the depletion capacitance

$$C_d = \frac{q}{k_B T} \tau_T I_d,$$

related to charge diffusion and storage effects in the bulk of the semiconductor, with τ_T being the minority carriers total transit time and I_d the forward current.

For lighting applications the value of I_d can be very high, thus the resulting intrinsic capacitance, $C = C_j + C_d$, of the device can be very large. By denoting the series resistance r_s, it is possible to calculate the diode time constant $\tau = r_s C$.

So the $-3dB$ electrical cut-off frequency of the device is

$$f_{el} = \frac{1}{2\pi\tau} \sim \frac{0.35}{\tau} \tag{2.2.2}$$

Common LEDs used for lighting show typical values in the $10 - 20\ MHz$ range, while VCSELs can go up to $> 10\ GHz$.

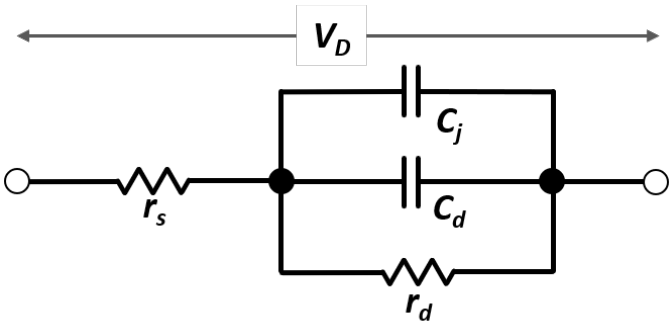

Figure 2.4: Diode forward bias equivalent circuit: V_d is the voltage applied to the diode, r_s is a general series resistance, r_d is the diode's resistance for small signals, C_j is the junction capacitance and C_d is the diffusion capacitance.

2.2.2 Light Emitting Diodes

The visible light, the region of the electromagnetic spectrum which is detectable by the human eye, ranges from approximately 380 nm and 780 nm, as presented in Fig. 2.5. Single-color LEDs are easy to obtain but lighting applications require a bright white light. The realization of a white LED source can take two different designs. The simpler and older version, named RGB-LED, is made by proportionally mixing red, green and blue LED chips together with combining optics to blend the three emissions. The human eye perceives this mixture as white light, unable to separate the single colors. Another design, named Phosphor LED (Ph-LED), uses a blue Gallium Nitride (GaN) LED coated by a Yttrium Aluminum Garnet (YAG) phosphor layer. The blue light emitted from the LED is partially absorbed by the phosphor layer that re-emits the light at a longer wavelengths, producing a white radiation.
In terms of electrical bandwidth, single colored LEDs, like those used in RGB design, have an approximated value of 12 MHz. In a Ph-LED, the slow response of the phosphor layer greatly limits the cut-off frequency to $2 - 3$ MHz, as demonstrated by the small-signal frequency response in Fig. 2.6. This two designs lead to distinctive optical spectra distributions $p(\lambda)$, the former Fig. 2.7 characterized by three separated peaks, one for each color, the latter shows the singular peak of the blue component together with the broad emission spectrum of the phosphors at higher wavelengths Fig. 2.8. It is clear, from Fig. 2.7 and Fig. 2.8, that LEDs's $p(\lambda)$

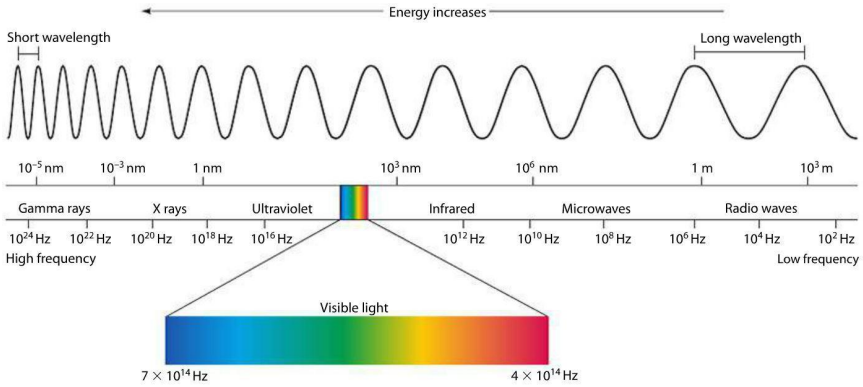

Figure 2.5: Classification of the electromagnetic spectrum as a function of radiation wavelength or frequency.

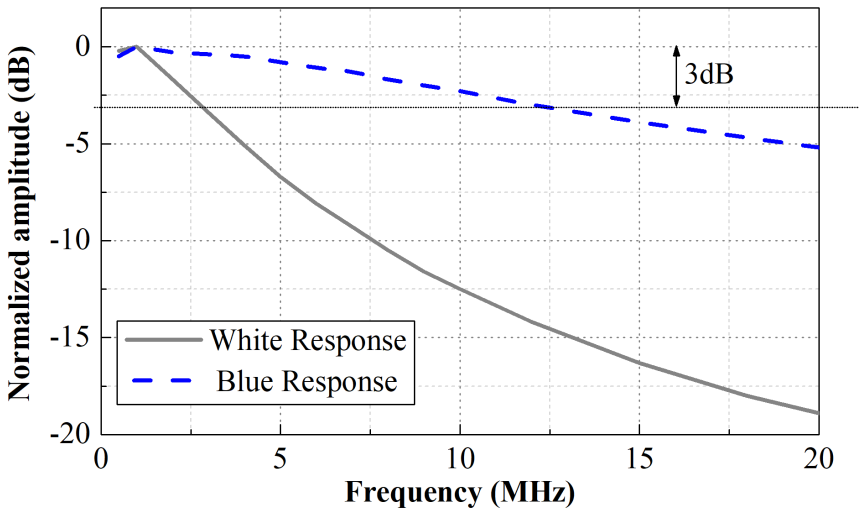

Figure 2.6: Normalized frequency response of a Ph-LED. The grey dashed line represent the response of the white light originating by the phosphor layer. The blue line is the original response of the blue LED below the phosphor, obtained by optically filtering the white emission.

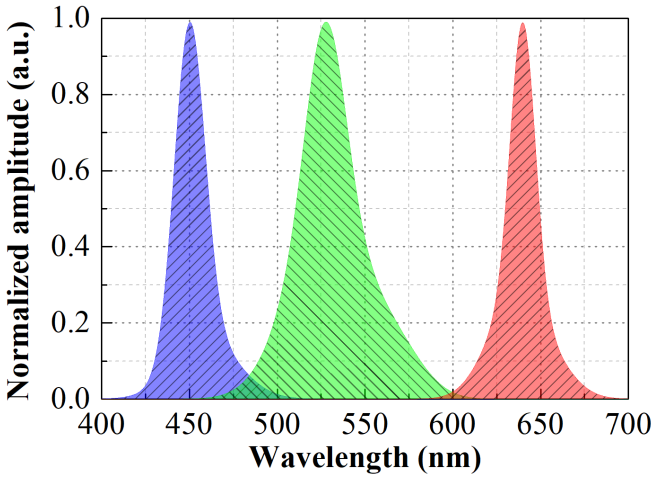

Figure 2.7: Normalized optical amplitude spectral distribution of a RGB-LED. The three peaks refer to the red (right), green (center) and blue (left) LED emissions.

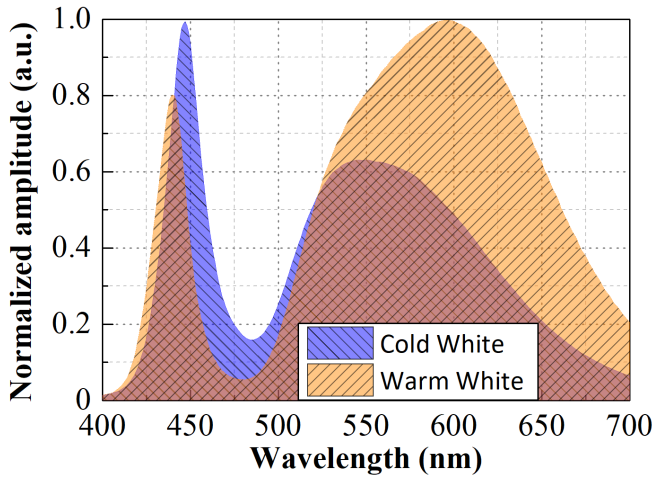

Figure 2.8: Normalized optical amplitude spectral distribution of a Ph-LED. Two different types of LEDs are presented, based on their Correlated Color Temperature: a cold white (higher 450 nm peak, in blue) and a warm white (higher 600 nm peak, in yellow) Ph-LEDs.

has a peaked emission with an optical bandwidth of $20 - 50\ nm$. This value is narrower than that of many common lighting sources (e.g. incandescent lamps) but still wider than monochromatic sources (e.g. lasers).

2.3 Receiving devices

In emitting diodes, light is produced by the radiative recombination of an electron-hole pair, in a transition between conduction and valence band. This generates a photon of a given wavelength, dependent on the energy gap. By using a different structure, a diode can also be used for the opposite process.
An impinging external photon is absorbed by an electron in the valence band giving it enough energy to move to the conduction band and generating an electron-hole pair. Applying an external field is then possible to move the charge carriers in the semiconductor and generate a current. This devices are called PDs and can be used for light detection by measuring the photogenerated current.
Although various other devices can be used for photon detection, e.g. phototubes or photomultipliers, here we will focus only on PDs, being the only devices covered in this thesis.

2.3.1 Positive-Intrinsic-Negative diodes

In Positive-Intrinsic-Negative (PIN) diodes, a region of undoped intrinsic semiconductor is introduced between two doped regions, P and N [17]. When reverse biased, the electrical field propagates through almost the entire intrinsic region. Thanks to photoelectric effect, absorbed photons create free charge carriers in the intrinsic region. Hence, a PD exposed to light generates a photocurrent due to the transport of these charge carriers.
As we have seen in Section 2.2.1, carrier transit time τ_T plays an important role in limiting the frequency response of PDs in optical communications. However, in order to increase the light harvesting capabilities of the RX, in OWC the employed devices have relatively large areas; that gives an increase of the device capacitance and hence reduces the PD's electrical frequency response.

2.3.2 Avalanche Photodiodes

The general structure of Avalanche Photodiodes (APDs) is very similar to that of PIN PDs, with the main difference being the number of electron-hole

pair generated for each absorbed photon. In APDs, the depletion region is designed to have a high electrical field in order to provide an acceleration to the generated carriers. Due to the augmented kinetic energy, the impact of the accelerated charge carrier with the semiconductor lattice creates new free charge carriers in the material. This field-induced avalanche effect multiplies the number of generated carriers per photon.
The main disadvantage of the avalanche process is the generation of an excess of shot noise caused by the amount of current flowing into the diode. In OWC, this effect combined with common high intensity ambient light, can degrade the quality of the signal, as explained in Section 2.4. Moreover, due to a non-unitary photocurrent gain, APDs show strong non-linear behaviour as a function of the incident optical power, unlike PINs that show an almost linear behaviour over a wide range of input optical intensities. For this reason, APDs are usually limited to applications that are more robust to their poor linearity, like in systems based on digital signals.

2.3.3 Camera Image Sensors

Camera Image Sensors (CISs), used in many applications, are constituted of arrays of photodetectors that can record not only the intensity of the light focused on it but a complete image. VLC system exploit the imaging capacity, together with the ability to distinguish different colors, to realize compact Multiple Input Multiple Output (MIMO) and Color Shift Keying (CSK) systems [18].
In these devices the technologies adopted are mainly two: the Complementary Metal Oxide Semiconductor (CMOS) and the semiconductor Charge-Coupled Device (CCD).
A CMOS sensor is based on an array of PIN PDs, while in CCD image sensor, p-doped Metal Oxide Semiconductors (MOS) capacitors are used as pixel light detectors. When the capacitor bias goes beyond the inversion threshold incoming photons are converted into electron charges at the semiconductor-oxide interface. The generated charge carriers are initially stored and then transported in a second step to a serial output register to extract the pixels information.
The two technologies also differ for pixel readout modes. CCD cameras often use Global Shutter (GS) readout mode, exposing simultaneously every pixel at the same instant. The signal from each pixel is transferred serially to a single Analog-to-Digital Converter (ADC) only after the complete frame has been exposed (Fig. 2.9). The delay introduced depends on the sensor size and limits the camera frame rate and hence the device bandwidth as opti-

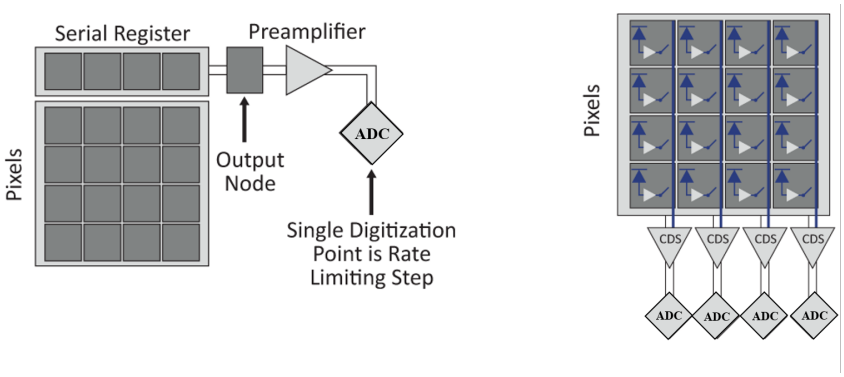

Figure 2.9: Basic schematics of CCD (left) and CMOS (right) sensor architectures.

cal receiver. The bottleneck related to ADC transfer is reduced in CMOS sensors in Rolling Shutter (RS) readout mode. In this mode, the system reads one row at time using an ADC for each line (Fig. 2.9). This means a smaller number of pixels to be digitized, shorter readout times and faster frame rates. A detailed description of the RS mechanism will be given in Chapter 4.

2.4 Channel properties

2.4.1 Optical channel model

In LED-based or low cost VCSEL OWC systems the only available modulation class is Intensity Modulation with Direct Detection (IM/DD) [19]. The OWC equivalent baseband model can be represented by the Eq. (2.4.1):

$$y(t) = R \cdot x(t) \otimes h(t) + n(t) \tag{2.4.1}$$

where a source of intensity $x(t)$ transmits through an Additive Gaussian White Noise (AWGN) channel with impulse response $h(t)$ and a signal-independent shot noise $n(t)$. The optical signal is then received by an optical RX with responsivity R, generating a photocurrent $y(t)$.
In OWC systems, $x(t)$ represents the power, not the amplitude of the signal as in RF systems, because the instantaneous optical power emitted is proportional to the generated current. The consequence of this property are two major constrains on these systems that differ from radio or electrical

communication systems: The quantity $x(t)$ must be non-negative

$$x(t) \geq 0, \forall t \tag{2.4.2}$$

and, for some applications, there could be limitations on the maximum usable optical power P_{max}, due to eye safety requirements. So, the average amount of allowed power P_{ave} is limited to

$$P_{ave}^{OWC} = \lim_{T\to\infty} \frac{1}{2T} \int_{-T}^{T} |x(t)|dt \leq P_{max} \tag{2.4.3}$$

Now, regarding the frequency response of the channel $H(f)$, the most important parameter is the gain at Direct Current (DC), $H(0)$, since the channel response is almost flat around it. For a general channel constituted by TX, RX and the transmission medium the DC response can be modeled as the product of the contribution of the three elements.

Transmitter model

A LED source follows the generalized Lambert Law [16]:

$$I(\phi) = I_0 \frac{m+1}{2\pi} \cos^m \phi \tag{2.4.4}$$

with reference with the simple geometry expressed in Fig. 2.10 where $I_0 = I(0)$ is such that:

$$\int_0^{\frac{\pi}{2}} \int_0^{2\pi} I_0 \cos^m(\phi) \sin(\phi) \mathrm{d}\phi \mathrm{d}\theta = 1 \tag{2.4.5}$$

in order to normalize the radiation pattern. The index m is the Lambertian radiation index of the source

$$m = -\frac{ln2}{ln(\cos \phi_{1/2})} \tag{2.4.6}$$

where $\phi_{1/2}$ is the source radiation semi-angle at half-power. Taking into account also the effect of the propagation distance, we obtain the contribution of the transmitter to the channel DC gain for a Lambertian source:

$$H_{TX} = \frac{m+1}{2\pi} \cos^m \phi \frac{1}{d^2} \tag{2.4.7}$$

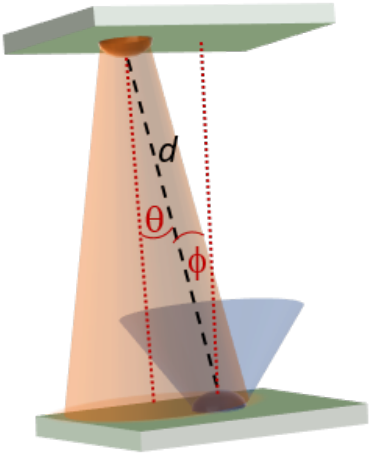

Figure 2.10: Simple scheme of free-space propagation of light: d is the distance between transmitter and receiver, θ is the emission angle of the transmitter and ϕ is the acceptance angle of the receiver.

Receiver model

In order to elaborate an accurate model for a general receiver, let's consider an arbitrary photodetector with active area A_{RX} and FOV of angle 2ψ. Accounting for the presence of an optical filter $f(\psi)$ and an optical concentrator of gain $g(\psi)$, the impact of the receiver can be modeled as:

$$H_{RX}(0) = A_{RX} f(\psi) g(\psi) \cos\psi \tag{2.4.8}$$

Transmission medium model

Light travelling through a medium different from vacuum suffers an attenuation. The impact of the transmission medium on light propagation can be described by the Beer-Lambert law [20]:

$$T(\lambda) = e^{-k(\lambda)d} \tag{2.4.9}$$

where the transmittance $T(\lambda)$ is the portion of the incident optical power, with wavelength λ transmitted through the medium, d is the material thickness and $k(\lambda)$ is defined as the **attenuation coefficient**. The Eq. (2.4.9) is valid only for a uniform and isotropic medium with $k(\lambda) = a(\lambda) + b(\lambda)$, where $a(\lambda)$ is the **absorption coefficient** and $b(\lambda)$ is the **scattering coefficient** of the medium. Since the coefficient k for clear air is very small, its impact is relevant only for d in the order of kilometers. For this reason,

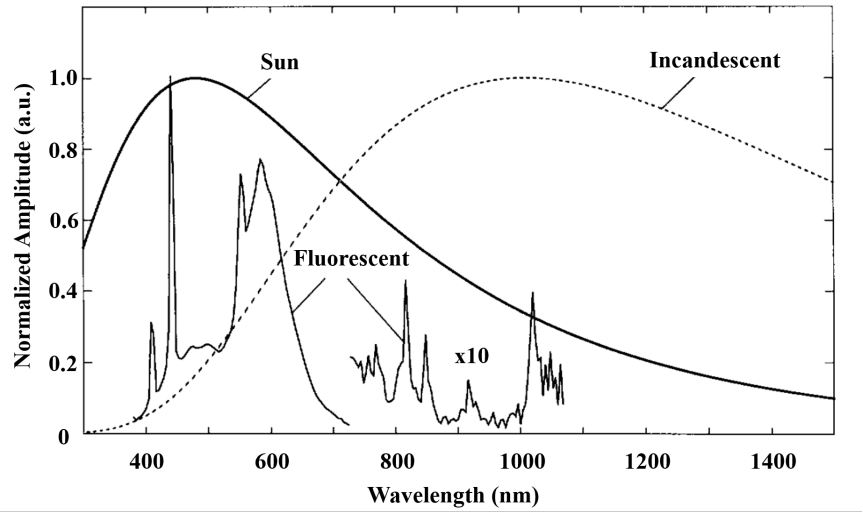

Figure 2.11: Optical spectra of background light sources

in the practical experiments conducted in air that are presented in the next chapters, the impact of the transmission medium will not be considered.
In conclusion, for a source emitting a signal with optical power P_{TX}, the received signal power can be written as:

$$P_{RX}(\lambda) = H_{TX}T(\lambda)H_{RX}P_{TX}(\lambda) \tag{2.4.10}$$

2.4.2 Optical noise sources

In a optical wireless channel the background light represents the main source of optical noise, in particular for systems with wide FOV RX. Depending on the nature of the background light, the impact on the transmission channel can be significantly different. It is possible to distinguish three noise sources classes (see Fig. 2.11): sunlight, incandescent and fluorescent lamps. The sun emits an unmodulated radiation over a broad spectrum, spanning from ultraviolet to near-infrared wavelengths. The impact of unmodulated light on the channel is the creation of a shot noise current at the receiver with a Root-Mean-Square (RMS) amplitude proportional to the incident optical power.
Incandescence lights, usually don't need any driving electronics and so are directly connected to the power grid for supply. The light emitted is then modulated as an almost perfect sinusoid dependent on the Alternating Current (AC) grid frequency, with all the harmonics over 800 Hz being 60 dB

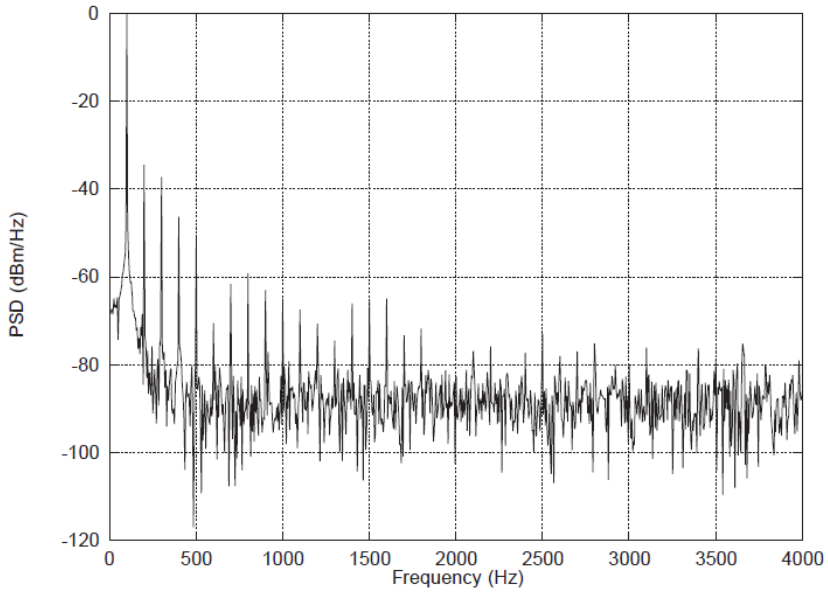

Figure 2.12: Typical interference spectrum of an incandescent lamp

lower than the fundamental frequency (see Fig. 2.12) [21].
Since in OWC systems the receiver has a much broader bandwidth this photocurrent is usually taken into account as a constant RMS shot noise, likewise to sunlight [19]. Fluorescent light sources, i.e. fluorescent tubes, generally require driving electronics that modulate their intensity. This induced modulation can vary with frequencies that can be equal to that of the power grid (alike incandescent lights) or can reach up to hundreds of kHz (see Fig. 2.13). The latter demonstrates a particularly negative impact in low-rate systems using On-Off Keying (OOK) or Amplitude Shift Keying (ASK) modulation formats [21]. These modulation show a strong DC component in their electrical power spectrum and this kind of noise cannot be filtered out without affecting considerably the signal.

Noise management

A general solution to reduce the impact of background light on OWC systems is the reduction of the RX FOV. However, in those cases where a wide acceptance angle is needed (see Section 2.1), other solutions must be taken into account. With the exception of optical transmitters with a wide emission spectrum (e.g. white LEDs), optical narrow-band filters can also

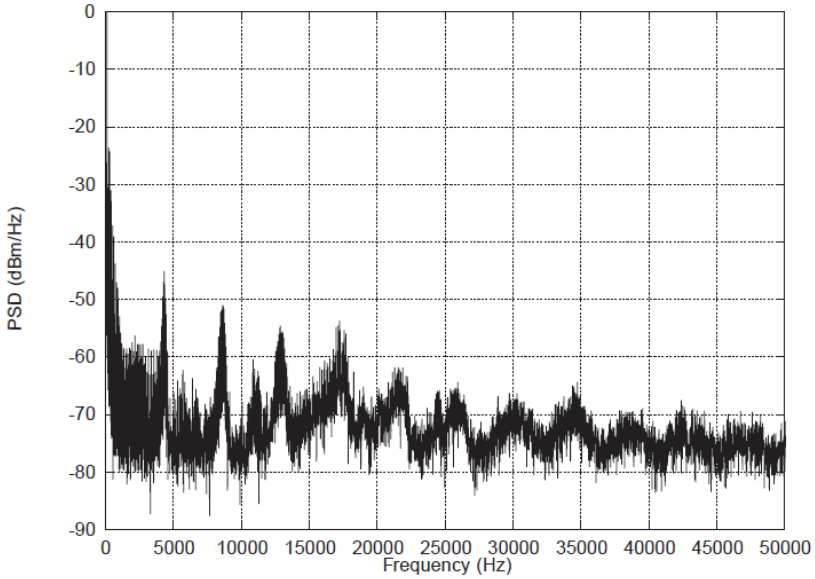

Figure 2.13: Typical interference spectrum of an fluorescent lamp

be employed to act selectively on the noise that is out of the transmission wavelength, with no impact on the received signal quality. A more specific analysis on the use of optical filter will be presented in Chapter 3. In addition, some of the background sources listed are modulated with a specific frequency (e.g. $\simeq 100$ kHz for fluorescent tubes). When the peak frequency of the noise is inside the signal bandwidth, the background cannot be modeled as an AWGN source. In these cases, software or hardware filtering should be applied on the received signal to mitigate its impact on system performance. This type of noise can be faced by using high-pass filtering in high-rate OOK/ASK modulations that have broad spectrum. Alternatively, it is possible to bypass the issue by using a bandpass signal or multiple-carrier systems, avoiding the affected frequencies.

2.5 Modulation formats

In OWC systems intensity modulation formats are the most used due to the constrains on the nature of the signal $x(t)$, as expressed in Section 2.4.1. Many aspects pose a relevant constrain on the allowed transmission power, such as power consumption limitations, eye safety and illumination require-

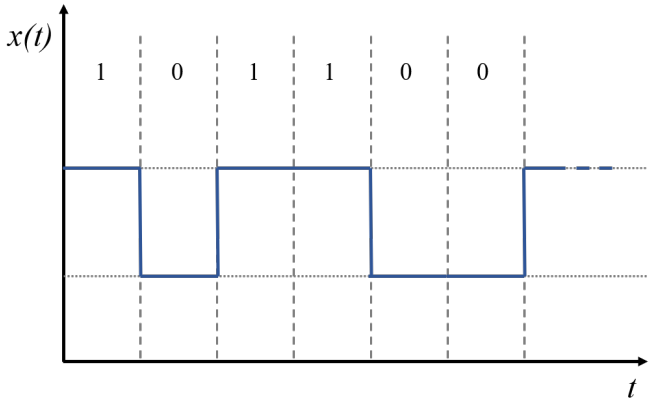

Figure 2.14: NRZ signal in the time domain.

ments. In OWC systems both single carrier and multiple carrier modulation formats are used depending on the requested performances or channel conditions. The systems presented in this thesis will mostly rely on single carrier modulations like OOK.
OOK is among the most used modulation formats, being the easiest to implement in practical applications, with a relatively good compromise between complexity and performance.
In OOK a single carrier intensity is modulated on the time scale, with a binary signal based on two different intensities, namely *low* state and *high* state, used to convey the information. From the relationship between the duration of the pulse representing a single state and the bit time we can distinguish different classes of OOK coding: Non-Return to Zero (NRZ), Return to Zero (RZ) and DC-balanced.

2.5.1 Non-Return to Zero

OOK-NRZ represents the most basic modulation format, where the signal pulse, representing the logical state, lasts for the whole bit time (see Fig. 2.14). This class is usually used as reference for other coding formats, due to its simplicity. In the design of an optimum receiver for these codes, considering an AWGN channel, it is possible to use a simple matched filter followed by a threshold detector. The detector threshold can be easily set to the mid-value between the two logical states. In this thesis, OOK-NRZ modulation was used in the experimental realization presented in Chapter 4. Here the format was chosen due to many factors:

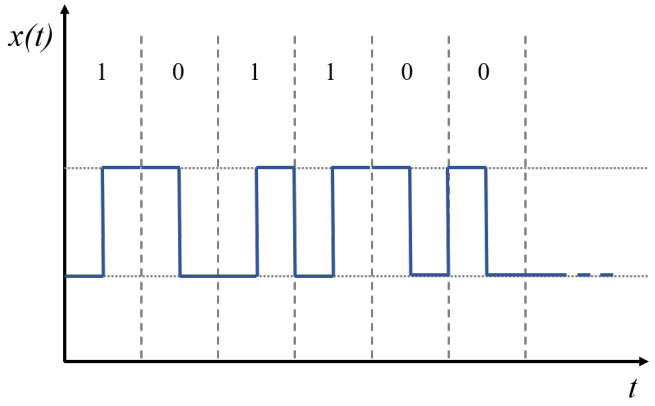

Figure 2.15: Manchester coded signal in the time domain.

- Simplicity of implementation
- The use of a image recognition algorithm allowed to select only the source excluding the background low frequency noise
- Presence of heavy waveform distortion with complex signal recovery for other modulation formats.

2.5.2 DC-balanced modulations

DC-balanced codes are usually defined as binary sequences with null value at zero frequency. Due to this feature, this class of codes, when applied to OWC, can counter the effect of low-frequency noise from ambient sources and help in mitigating the impact of frequency cut-off of AC-coupled components in the system (e.g. amplifiers, bias-tees, etc.). Among the most popular DC-balanced codes there are Manchester coding and block codes. A Manchester code encodes each bit in a transition between two states and removing the presence of a DC component in the signal (see Fig. 2.15). In order to generate the signal a binary XOR is used to combine a NRZ data with a clock signal with a frequency that is the double of the binary signal. The resulting signal has then an embedded clock that improves signal synchronization and clock recovery. While these characteristics are very attractive, it should be noted that they are obtained by doubling the bandwidth occupation and hence reducing the spectral efficiency, as showed in Fig. 2.16. A better coding efficiency can be achieved by using block codes. In block codes, the information is grouped in m-digits codewords that are

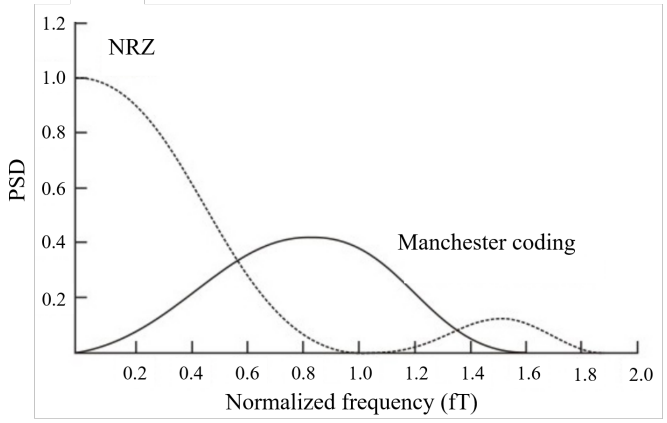

Figure 2.16: Compared PSD of NRZ and Manchester coded signal in the time domain.

translated in n-digits codewords, with $n > m$, by the use of a conversion table (*codebook*). Mapping the information on a wider basis allows the implementation of additional rules on possible bit sequences, e.g. the minimum number of state transitions in each word. In order to have a comparison, let's consider the 8B/10B block code, one of the most used, i.e. in Gigabit Ethernet standard [22]. In this case the code requires a 25% extra bandwidth, compared to 100% extra bandwidth needed for Manchester coding. While block codes are more bandwidth-efficient than Manchester codes, this advantage is achieved at the cost of a reduced efficacy in low-frequency components management. Manchester coding is the modulation scheme of Ethernet 10Base-T standard, implemented in this thesis for indoor (Chapter 3) and underwater (Chapter 5) VLC systems. The choice here, both cases, was driven by the use of a widely adopted standard. We selected the Ethernet standard to address the need of a medium bit rate (10 $Mbit/s$) for video and high definition image transmission. Further details will be provided in the relative chapters.

Chapter 3

Embedded VLC indoor transmission system

3.1 State of the art

In the last years, Gigabit-class D-LOS systems played a leading role in research on VLC. To achieve Gigabit rates, LED-based VLC systems require, due to bandwidth limitations, a mix of complex modulation schemes, ad-hoc devices or signal pre-distortion [23].
Moreover, LED Gigabit systems are usually limited to D-LOS configuration, which benefits from the highest achievable Signal-to-Noise Ratio (SNR) and thus also the fastest bit rates. However, these systems need beam collimation and precise alignment, two features that do not match well with the required mobility of commercial mobile devices. In addition, D-LOS communications are greatly affected by various other limitations, such as LOS interruption and shadowing.
All these factors represent currently a critical barrier in bringing the VLC D-LOS technology from academia to commercial solutions.
As seen in Chapter 2, the beam spread of a ND-LOS TX can be much wider than in D-LOS configuration, relaxing the constrains on alignment and improving RX mobility without any signal tracking system [19] [24] [25]. The downside of this feature is a relevant reduction in SNR due to the limited optical power collected at the RX and a huge increase in received ambient light. Ambient light not only can deliver a consistent amount of noise in the channel but it can saturate the PD at RX reducing its sensitivity.
Nonetheless, while the achievable data rate for ND-LOS VLC systems is strongly limited by their characteristics, on the short therm they represent

the best trade-off to deliver VLC technology in commercial devices.
In 2013, Cossu et al. [26] achieved a 200 $Mbit/s$ indoor transmission over an area of 2.4 m^2 radius, using Discrete Multi-Tone (DMT) modulation and Wavelength Division Multiplexing (WDM) over a RGB-LED in a ND-LOS configuration.
In 2014 they [27] demonstrated experimentally an indoor VLC system in a ND-LOS configuration, achieving a 250 $Mbit/s$ bit rate over a link span of 2 m. The system was also able to provide a 100 $Mbit/s$ minimum rate over a 12 m^2 area. The same authors upgraded the system in [28], achieving a new transmission rate of 400 $Mbit/s$. The proposed system exploited a carefully selected LED/optical filter couple and offline Digital Signal Processing (DSP).
In 2015, Brandl et al. [29] demonstrated a 1 $Gbit/s$ link at a distance of 3.3 m, using a custom APD and achieving a Bit Error Ratio (BER)$< 10^{-9}$ with an acceptance angle of 68 degrees.
In 2018, Chen et al. [30] demonstrated experimentally the realization of an hybrid VLC-Infrared (IR) system, with a transceiver using multiple PDs and LEDs to achieve omnidirectional communication robust to mobile devices rotation.
All the listed systems show interesting performance in a laboratory environment. Moreover the presented solutions are all self-standing realization that could be hardly integrated in pre-existing infrastructures and, hence, their deployability in a real scenario. Here we present a VLC system implemented in a commercial table lamp, with no changes to the embedded Ph-LED; we upgraded the lamp through an in-line VLC system implementing an Ethernet 10BaseT signal over the emitted light. We characterized the system by a real-time transmission of a 12.5 $Mbit/s$ Manchester coded signal, emulating the physical layer of a 10Base-T Ethernet and by measuring the packet losses. We estimated an angular tolerance to misalignment exceeding ± 45 degrees: no packet loss was observed up to 93 cm of horizontal displacement in a ND-LOS link (covered area of 2.7 m^2). The system shows excellent robustness even in highly illuminated environments.
The author would like to highlight that his contribution to the system presented in this chapter relates to its complete design, characterization and test.

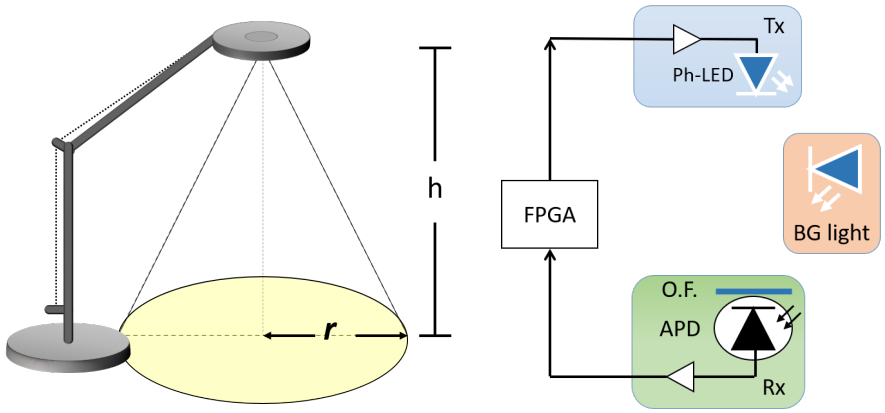

(a) (b)

Figure 3.1: Experimental setup of the VLC system:a)Spatial parameters used in the tests, h is the vertical TX-RX distance and r is the horizontal radial distance from the light emission central point; b)Setup scheme, an FPGA is used to generate a 12.5 $Mbit/s$ Manchester signal and evaluate the system BER, a Ph-LED with an amplifier constituted the TX, an APD with an Optical Filter (O.F.) and an amplifying stage constituted the RX, cold and warm white LEDs were then used to simulate background (BG) light.

3.2 System setup

The main purpose of this activity was to demonstrate the feasibility of a VLC system that could be readily implemented in common lighting equipment in a plug-and-play fashion and support a standard protocol (Ethernet) with no need for additional conversions. We have modeled the experimental setup as a common working scenario, employing a tabletop LED lamp with a fixed height $h = 85\ cm$, providing at least an illuminance of 500 lx at desktop level over a radial distance r of at least 0.75 m (Fig. 3.1a), in compliance with the European standard for indoor working environments [31]. The setup scheme is sketched in Fig. 3.1b. In order to add VLC capabilities to the lamp, the driving electrical signal and a DC bias were combined by means of a bias-tee. To execute a BER measurement on the system, we used an Field-Programmable Gate Array (FPGA) (Xilinx, 7) as both Pseudo Random Bit Sequence (PRBS) generator and BER-tester. We generated a signal equivalent to 10Base-T Ethernet physical layer signal producing a Manchester-coded PRBS at 12.5 $Mbit/s$. At RX side, a blue filter was used

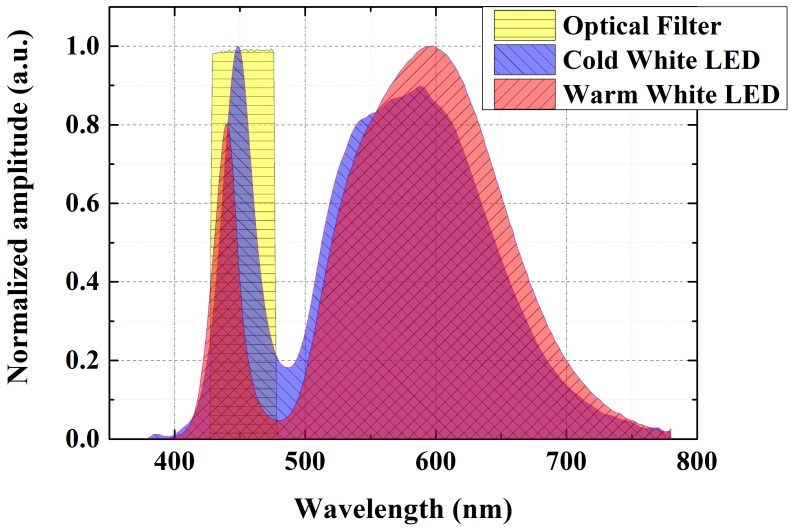

Figure 3.2: Optical spectra of the Ph-LED used superimposed to the transmittance band of the RX optical filter.

to filter out the slow phosphorescent components of the light ($\lambda = 460\ nm$ central wavelength, $\sim 50\ nm$ optical bandwidth and $> 90\%$ transmittance), to detect only the fast-modulated spectral region (see Section 2.2.2). As part of the RX we used a silicon APD (1 cm^2 active area, 11 MHz bandwidth, responsivity of 0.23 A/W at $\lambda = 450\ nm$). To achieve compliance with commercial Ethernet interface cards, electrical amplifiers were used to match the expected signal amplitude (2.5 V) at both the TX and RX sides. VLC systems are known to be strongly affected by the Background (BG) illumination, which can saturate the RX and/or induce additional photo detection noise [32]. To measure the effect of the BG light we placed the system in a dark environment to avoid disturbance by the laboratory illumination. Using two auxiliary LEDs (unmodulated), alternatively, we emulated a BG illumination of controlled level. We selected two devices emitting a white optical spectrum with a Correlated Color Temperature (CCT) of 2900 K and 4100 K, respectively. We made this choice to account for different types of ambient lights, which may be either "warm" or "cold" white lighting equipment. We report the spectral distribution of the light emitted from the Ph-LEDs, superimposed with the transmittance bandwidth of the optical filter, in Fig. 3.2.

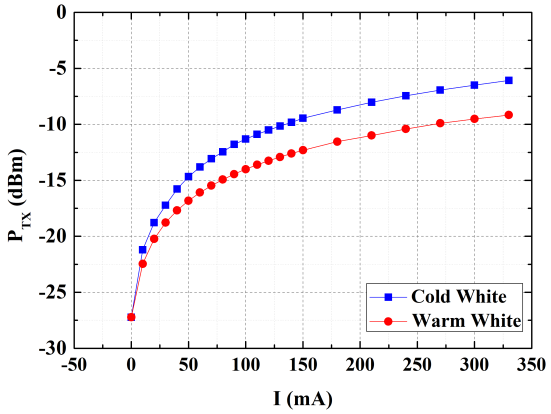

Figure 3.3: Optical power at the TX side P_{TX} vs current I curve for cold and warm white LEDs.

3.3 System characterization

To perform the VLC system implementation, the LED embedded in the tabletop lamp, together with the complete communication system, must be characterized in both its optical and electrical properties. The LED embedded in the tabletop lamp is the same model as the one used to emulate the cold white BG illumination. The emitted optical power at the TX side P_{TX} as a function of the supply current I is reported in Fig. 3.3 for both the cold and warm white LEDs.

As reported in the previous section, the system comprises an optical bandpass filter centered around the 450 nm wavelength. However, interference filters have a transmittance spectrum that depends upon the angle of incidence of light. The change is not only related to position and amplitude of the transmittance band, but can alter also its shape in a complex way. Therefore, for systems in ND-LOS configuration, there is an additional contribution due to the change in the transmittance band of the filter with the incidence angle of the light. This effect impacts both the TX and the BG LEDs, requiring a complex setup to have two different controlled angles for both sources. To address this issue, we implemented the attenuation of the signal power at the RX side due to the behaviour of the optical filter with the angle. First we calculated its value by simulation and then we used several optical attenuators to account for it in the experimental setup. In order to decouple the angular dependence of LED Lambertian emission, see

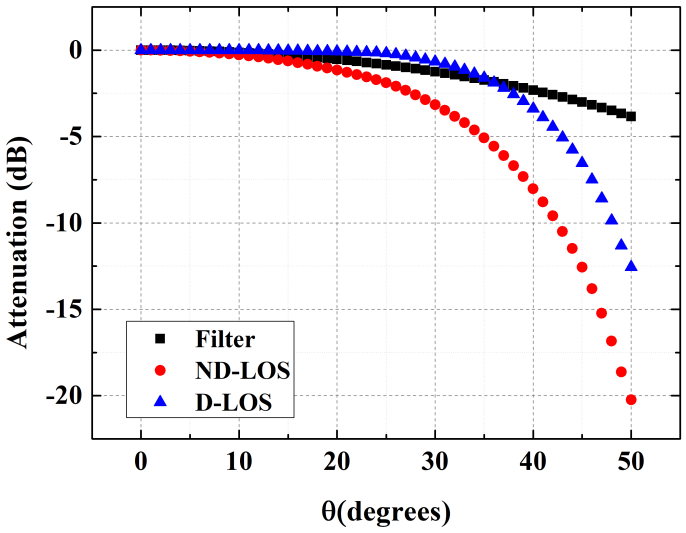

Figure 3.4: Optical attenuation at the RX side as a consequence of angular displacement. Optical filter attenuation profile in the transmitter optical bandwidth and the simulated attenuation on D-LOS and ND-LOS VLC systems as a function of the angular displacement.

Section 2.1 and Section 2.4.1, we simulated the impact of the angle for both D-LOS and ND-LOS configuration. In Fig. 3.4 are presented the optical attenuation at the RX side due to angular displacement. The attenuation is calculated as the integral of the attenuation over the transmission optical bandwidth, normalized with respect with the received optical power in the position at $\theta = 0$. In black is reported the angular attenuation of the filter, in blue the impact on D-LOS configuration and in red the impact on ND-LOS configuration. We computed the simulation for the ND-LOS in the case of $\phi = \theta$, when the RX is always facing in the direction perpendicular to the plane containing the transmitter. From these data it can be seen that the impact of the optical filter is higher in the ND-LOS configuration, as expected, halving the received optical power at 30 degrees, whilst the D-LOS configuration reaches the same attenuation at 40 degrees (see Section 2.4). We did not account for distance contribution to attenuation at this stage in order to solely focus on angle impact and simplify the calculus.
Finally, we measured the system bandwidth in the described setup, by using a LED bias current of 300 mA and a 1 Vpp signal amplitude before the

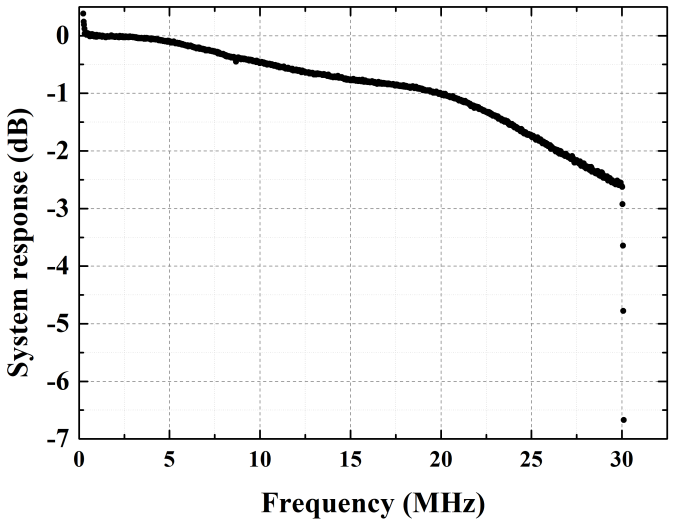

Figure 3.5: System response as a function of frequency. The system shows a 3dB-bandwidth of $\sim 30\ MHz$.

amplifying stage. We report in Fig. 3.5 the obtained system response as a function of frequency. These results show a measured 3dB-bandwidth of $\sim 30\ MHz$.

3.4 Impact of background light on BER

In order to measure the impact of the background light on the system we performed a BER test using a Manchester-coded signal with a fixed bit rate of 12.5 $Mbit/s$. The system parameters for test were the same as those used for the electrical bandwidth calculation, LED bias current of 300 mA and a 1 Vpp signal amplitude before the amplifying stage. The values of BER were first measured in aligned position ($r = 0$, $\theta = 0$), with a received power $P_{RX} = -14.7dBm$. In order to have a fair comparison of the different LEDs, P_{RX} and the background optical powers (P_{BG}) were measured after the optical filter. By applying optical attenuation at the TX side, we varied P_{RX} with no other influence on the system parameters. The variation of P_{BG} was obtained applying different values of bias current. Thanks to the methodology used, we can assume that the measured values of P_{RX} and P_{BG}

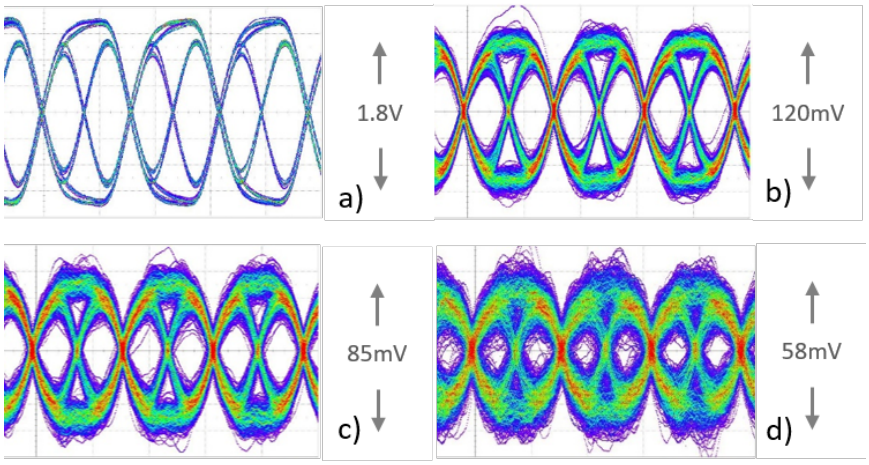

Figure 3.6: Eye-diagrams for different P_{RX}:
a) $P_{RX} = -14.7dBm$,(BER= 10^{-9});
b)$P_{RX} = -29.7dBm$ (BER= 10−7);
c) $P_{RX} = -31.7dBm$ (BER= 10−5);
d) $P_{RX} = -33.7dBm$ (BER= 10^{-3}).
In all cases, BG is non-negligible ($P_{BG} = -20\ dBm$).

were independent. The BG optical power measured at the RX side in dark condition (both signal and background LED were off) was $P_0 = -37.0\ dBm$. The impact of background light it is evident by the eye diagrams (Fig. 3.6) taken at different P_{RX} values for same P_{BG} ($-20\ dBm$). The shape of the eye diagrams is typical of a Manchester-coded OOK signal, where no more than two high (low) states can be consecutive. Eye closure, and hence signal degradation, are clearly seen as signal level goes lower and approaches that of the noise fluctuations. The results of the BER test as a function of P_{RX} in Fig. 3.7 show that the induced penalty from different P_{BG} for both BG sources has a maximum value of $\sim 6\ dB$ for the worst case of $P_{BG} = -9.9\ dBm$. We assumed 10^{-9} as our target BER value since no error correction code was implemented. It can be clearly seen that the system achieves the target BER even with P_{BG} 10 dB higher than P_{RX}. This indicates the strong robustness of the system. Data with BER$< 10^{-9}$ have not been measured since were not relevant for this study.
From these data we can extract the system sensitivity as a function of BG light, which is reported in Fig. 3.8. In the graph the two vertical lines mark the threshold value of 500 lx illuminance for the different BG LEDs. Nat-

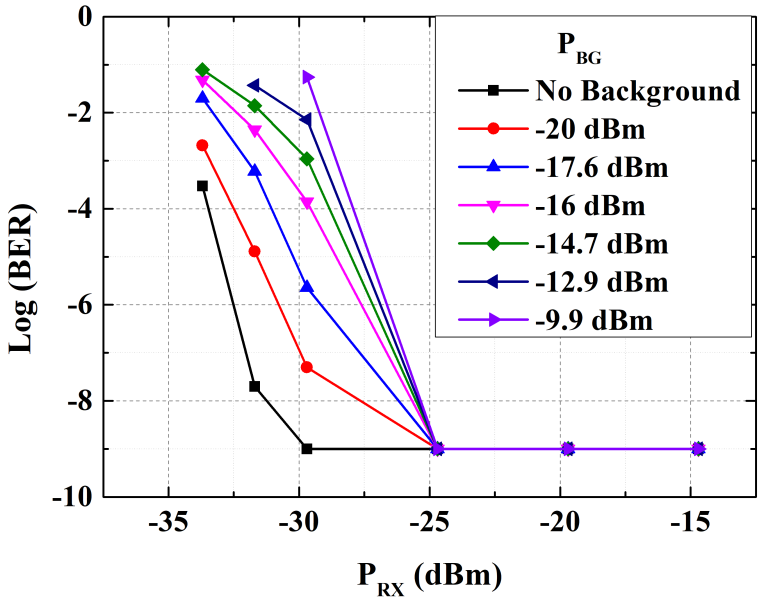

(a) Cold white background light

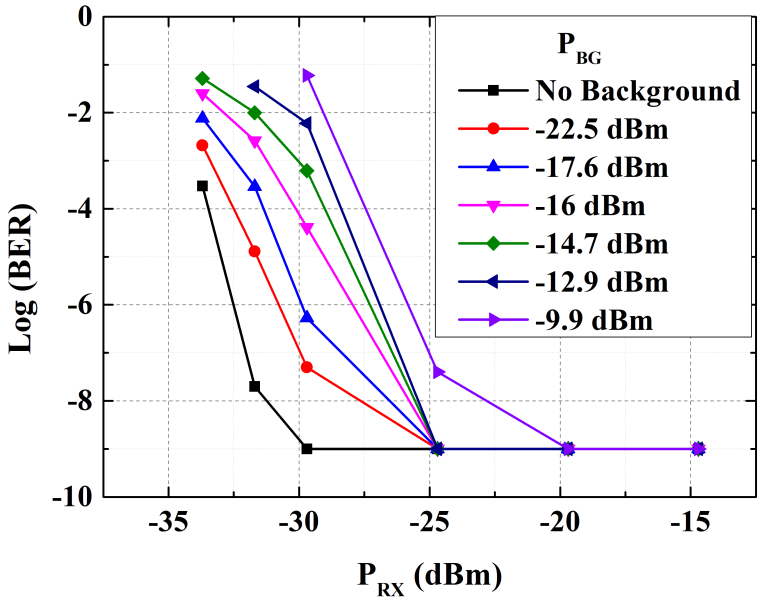

(b) Warm white background light

Figure 3.7: BER test of the system as a function of P_{RX} in different background conditions, BER target is 10^{-9} since no error correction code was implemented. In both graphs the maximum penalty for $P_{BG} = -9.9dBm$ is $\sim 6dB$.

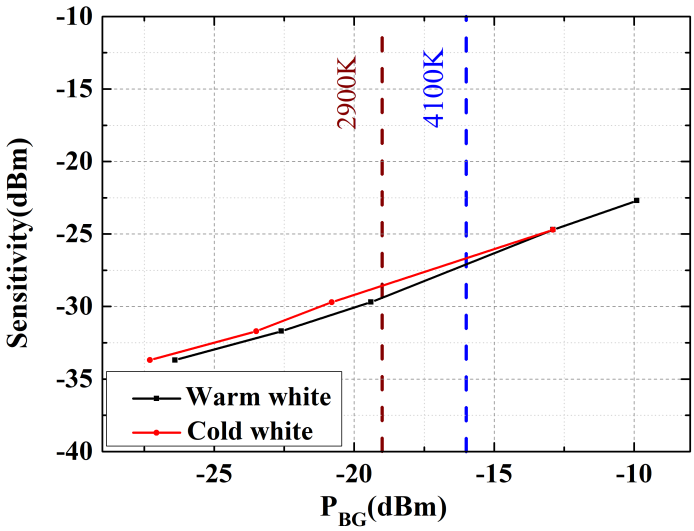

Figure 3.8: System sensitivity at target BER 10^{-9}. The two vertical lines mark the threshold value of 500 lx illuminance for the two LEDs with different CCT.

urally, for the LED with lower CCT, the filtering effect is stronger, thus at same illuminance threshold the two BG sources have different P_{BG} values of $-16\ dBm$ and $-19\ dBm$ for the cold and warm white light, respectively. As expected in the selected scale, the data show a linear dependence between sensitivity and P_{BG}. As expected, when P_{BG} increases the sensitivity decreases.
As already said in Section 3.3, the interference filters have narrow bandwidth that is dependent on the incident angle of the light. The angular dependence of our filter can make very difficult to accurately measure the fraction of BG light detected at every position; thus we decided to estimate the expected system behavior in ND-LOS as in [33] instead of resorting to more complex experimental setups. Given the measured system parameters, we report in Fig. 3.9 the maximum achievable radial distance r as a function of P_{BG} (considering the target BER= 10^{-9}). In the calculation, we accounted for a ND-LOS configuration with equal angle of emission from the transmitter (θ) and of incidence on the RX (ϕ). The results show that the system can reach a minimum distance $r = 63cm$ with strong BG illumination ($P_{BG} = -10dBm$, 3000 lx) and a maximum achievable distance of $r = 93cm$ at $P_{BG} < -27.3dBm$, corresponding to a maximum coverage area of 2.7 m^2 over a circle, centered on the lamp. From these values, we can estimated a maximum displacement of ~ 47 degrees.

3.5 Ethernet transmission

In order to confirm the estimated coverage data, we tested the system with Ethernet transmission. For this test, we realized a point-to-point link between two PCs using the VLC system as a wireless bridge, connecting the Ethernet network interface cards by CAT5 cables with RJ-45 connectors to the VLC TX and RX, respectively. A 10Base-T Ethernet transmission was realized, using the UDP protocol (see Fig. 3.10) between the two PCs. We ran two different experimental tests. In the first test, we used a random packet generator to produce Ethernet traffic and measured the packet loss as a function of the radial distance r for different value of P_{BG} with both cold and warm white light background: we sent a total of $\sim 122,000$ packets, with a packet size of 1 $kByte$ for different r values. The results, presented in Fig. 3.11 confirmed the BER analysis, showing zero packet loss up to the maximum distance limit calculated previously ($r = 93cm$). In the second test, high-quality video streaming (720p) was successfully carried out; we transmitted various video files from one PC to the other with no quality

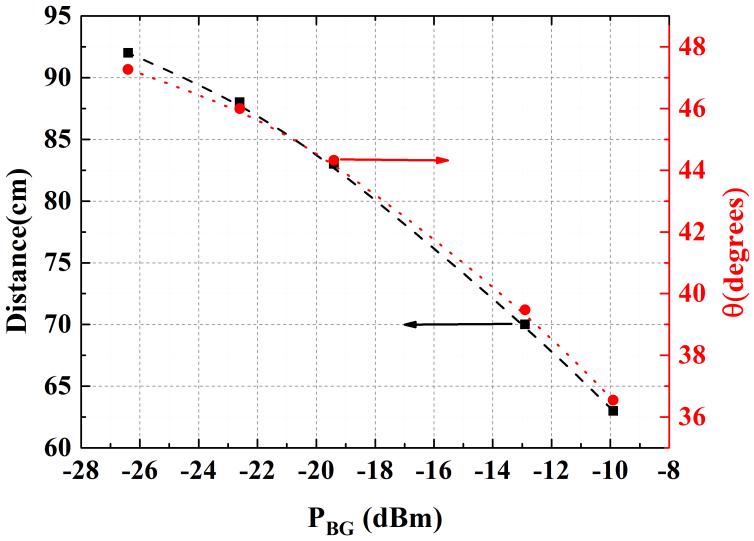

Figure 3.9: Tolerance to horizontal (black) and angular (red) displacement as function of BG light (all values taken at BER= 10^{-9}

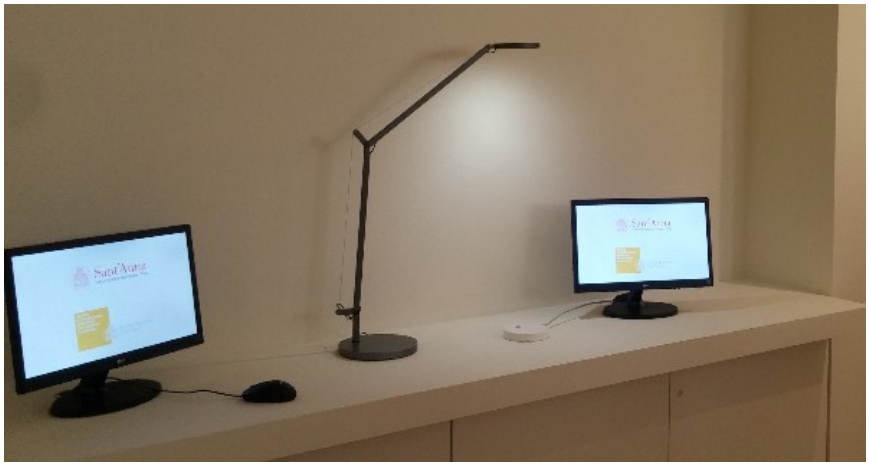

Figure 3.10: Experimental setup for Ethernet test over VLC link

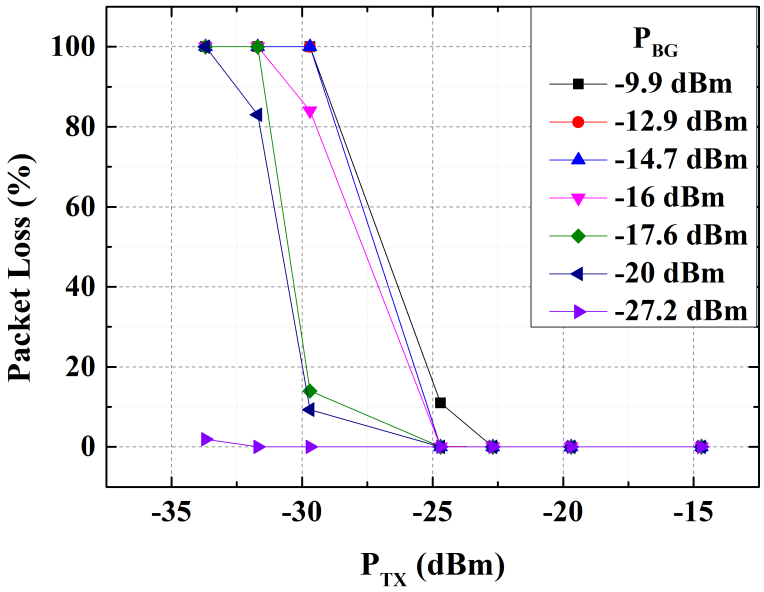

(a) Cold white background light

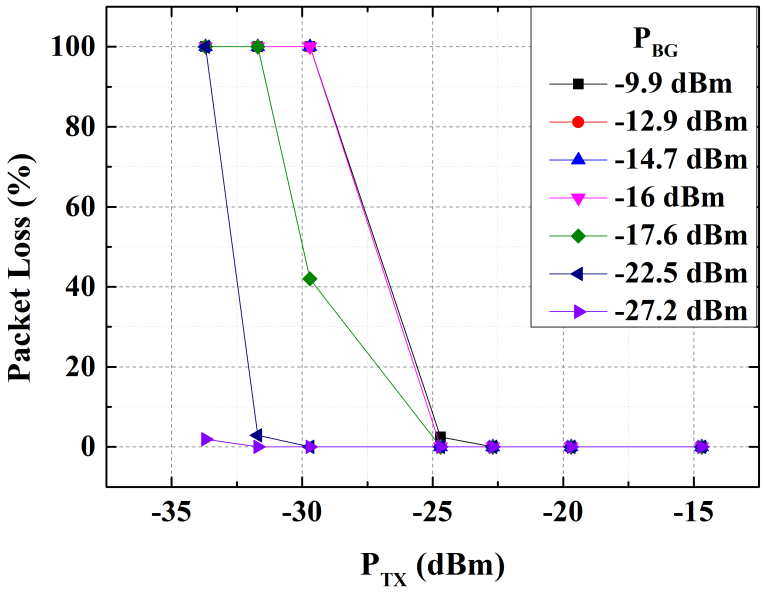

(b) Warm white background light

Figure 3.11: Packet-loss test of the system as a function of P_{TX} in different background conditions. The test confirmed the calculated results for the maximum achievable distance ($r = 93cm$) obtained by the previous tests.

degradation or increased delay up to the maximum distance. The video was broadcasted using UDP protocol and received using VLC media player software to reproduce it.

Chapter 4

Optical Camera Communications

VLC represent a mature technology that is still struggling to find a mass deployment. As showed in [4], LEDs mass adoption is a ongoing process which gives an enormous potential for VLC transmitters diffusion. At the same time, the need of custom receivers for light detection can lead to issues due to device availability, hindering the development of VLC solutions. However, while PD-based receivers do not represent widespread devices, digital cameras are part of the common everyday experience.
This chapter will focus on the use of digital cameras in VLC systems, a technology also known as Optical Camera Communication (OCC). In particular we will show what are the issues related to this technology, how is possible to solve some of these with image processing, using both simulations and tests.
The author would like to highlight that his contribution to the system presented in this chapter relates to its complete design, characterization and test.

4.1 State of the art

Compared to PD-based VLC systems, OCC systems face a number of practical challenges, such as greater ambient noise, low data rates and mobility [34]. In OCC the limited number of frames per second (fps) of the camera represent one of the main limitations in data transmission. In some cases, high-end special cameras can reach up to thousands fps [35] [36].
However, as explained in detail later in the next section, full-frame sampling

is not the only solution in OCC. In [37], the authors increased the data rate up to several *kbps* by using the Rolling Shutter (RS) feature of digital cameras, a sampling technique used to recover the information recorded by the single rows on the CIS.
In [38], the authors used the RS to increase the maximum data rate to ~ 10 *kbps*.
As will be explained in the next section, the data rate in OCC systems depends on the link span, which is determined by the intensity of the observed TX as well as on the source image size. In fact, the maximum number of detectable signal samples depends on the number of pixels that fit inside the source projection on the CIS and hence the link span. This number multiplied by the camera fps gives then the total number of signal samples per second by the camera. However, when the TX geometrical projection on the CIS is smaller than the sensor surface, there is a part of the sensor that is not covered by the image of the TX and hence cannot sample the signal. Reading these empty lines still takes some time, reducing the sampling period of the camera to discontinuous sampling bursts. In case of a continuous transmitted signal, this gives and incomplete sampling and an information loss.
Although synchronized burst transmission can overcome this limitation, in a general deployment, different cameras may show different fps or sampling speed, depending on the manufacturers or on software constraints [39]. This may lead to poor synchronization and increased error rates. Moreover, OCC systems use the sum or the average of the pixels intensity on the same row to extract the signal from the picture. This operation introduces a signal distortion, due to the source shape and size which acts as an envelope of the signal [40]. In order to recover this distortion, in [37] and [40] the authors proposed the use of polynomial curves fitting. This strategy achieved good results for a link span of < 50 *cm*, still preventing its adoption in many real scenarios.
Alternatively, in [41] the authors proposed the use Region of Interest (RoI) detection to identify the TX for localization purposes but with no further use for data detection.
In this chapter, we present a novel approach to the use of RoI detection in RS-based OCC. As we will show, the knowledge of the source shape can be used to reduce signal distortion and design the packet flow to avoid the need for burst transmission and hence synchronization.

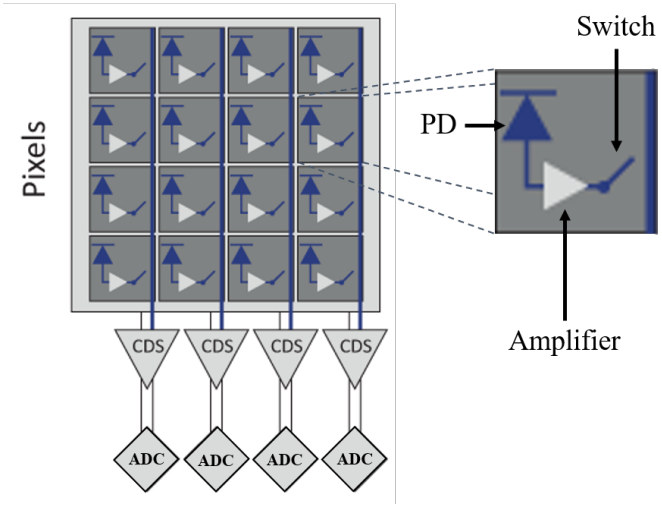

Figure 4.1: Schematic representation of a CMOS camera sensor. Each pixel (right) can be represented as a small circuit with a PD, an amplifier and a switch. The signal on each line (row or column) is sampled through a Correlation Double Sampler (CDS) and then digitized by an ADC.

4.2 Background theory

The two main technologies adopted in CIS are the Complementary Metal Oxide Semiconductor (CMOS) and the semiconductor Charge-Coupled Device (CCD). The former is more accurate and the latter is more power efficient and fast. The two technologies mostly rely on two readout methods: the Global Shutter (GS) mode used in CCD-based cameras; and the Rolling Shutter (RS) mode adopted in CMOS-based cameras [42]. In GS, the images are captured using all the pixels at the same time and the data is readout row-by-row. Differently, in the RS scheme the image capture on a row-by-row basis and the readout of the information is done after each row, in sequence. We will describe in details the RS mechanism in the next section, being the only readout method used in this thesis.

4.2.1 Rolling shutter mechanism

The structure of a CMOS camera image sensor is presented in Fig. 4.1. Here each pixel in a given row is a PD that simultaneously generates a photocurrent that is sampled by a Correlated Double Sampler (CDS) and then digitized by an ADC. In RS readout method, the pixels are sampled at

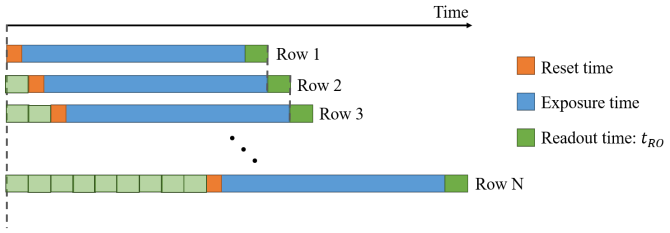

Figure 4.2: In Rolling Shutter readout mode, pixels integrate the amount of impinging light during an exposure time. The current each pixels of a given row are then sampled and digitized during the readout time. Since only one line at time can be digitized there is a reading delay equal to the readout time between two consecutive lines. After being read, each line is reset to be exposed again.

high-speed, row-by-row, instead of the whole array as in GS, introducing a small delay between rows of pixels. The timing of this mechanism is shown in Fig. 4.2:

1. the first row is exposed to the light impinging on the sensor for a time t_{exp}, being reset soon after;

2. the signal from each pixel of the row is then sampled and digitized, by dedicated CDSs and ADCs. This process require a readout time t_{RO};

Hence, each line is exposed with a t_{RO} delay related to the previous line. The total frame time for an N-lines sensor is then equal to $N \cdot t_{RO} + t_{exp}$. When there is a change in light conditions inside the captured scene, faster or equal to t_{RO}, darker and brighter rows appear superimposed on the image. In VLC systems the intensity of a light source is modulated to convey an optical signal. Analyzing the resulting pattern of dark and bright rows on a picture or a video of the optical source is possible to recover the transmitted signal. RS allows then the use of common CMOS cameras as optical receiver in VLC system with a sampling time equal to t_{RO}.
Picture parameters, such as the exposure time t_{exp} and the ISO value, affect the quality of the signal. The exposure time t_{exp} is the time interval over which the each pixel of a row integrates the received light and is then related to the value of the photogenerated current by each pixel. The ISO value measures the amplification gain applied to the photocurrent of each pixel.
In [41], Kuo et al. showed that, using an OOK modulation, the minimum t_{exp} achieved the best separation between the levels, in particular with strong

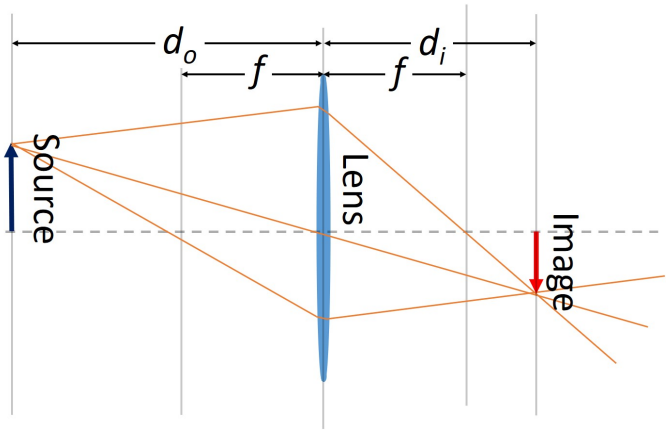

Figure 4.3: Object projection with a biconvex lens.

direct light to avoid pixels' saturation or the "blooming" effect. Therefore, for signal extraction the best camera parameters are the lowest available t_{exp} and the ISO of the device.

4.2.2 Pin-hole camera model

As seen in the previous section, to optimize the signal detection is necessary to use minimum t_{exp} and ISO. However, in this condition the light source used as the TX represent the only visible object in the picture. This limits the number of sensor rows that can sample the signal to those covered by the source projection on the CIS. The RX experiences a blind period of duration $t_{RO} \cdot N_{lost}$, where N_{lost} is the number of rows that are out of projection. Using a simple pin-hole camera model with a biconvex lens (see Fig. 4.3), we can calculate the impact of source distance on its projection on the CIS and hence the throughput loss $T_{\%}$ in the blind period of the RX. With reference to Fig. 4.3 the *thin lens formula* states that:

$$\frac{1}{d_o} + \frac{1}{d_i} = \frac{1}{f} \tag{4.2.1}$$

where d_o, d_i and f are the object-lens, lens-image and focal distance, respectively. Moreover, for a lens of magnification M

$$M = -\frac{d_i}{d_o} = \frac{S_i}{S_o} \tag{4.2.2}$$

where S_i and S_o are the image and object sizes perpendicular to the optical axis. So by considering Eq. (4.2.2) and noting that for a focused camera $d_i =$

f, and denoting the link span as d the source projection on CIS becomes:

$$S_i = \frac{f}{d} \cdot S_o \tag{4.2.3}$$

and considering a pixel size of s_{px}, the number of maximum signal samples as a function of distance is

$$N_{samples}(d) = \frac{f \cdot S_o}{d \cdot s_{px}} \tag{4.2.4}$$

Given a total number of rows in the CIS equal to N_{tot} the number of samples lost being out of projection is

$$N_{lost}(d) = N_{tot} - N_{samples}(d) \tag{4.2.5}$$

Considering an OOK-NRZ modulation, for a bit time t_b the number of samples per bit is

$$N_{spb} = \frac{t_b}{t_{RO}} \tag{4.2.6}$$

Considering Eq. (4.2.5), Eq. (4.2.6) and a transmission rate R_{TX}, the throughput loss as a function of distance in OCC channel for each frame is

$$T_{\%}(d) = \frac{N_{lost}(d)}{N_{spb} \cdot R_{TX}} \cdot 100$$

From Section 4.2.2 we can see that the system throughput decrease with distance d as $1/d$, introducing an information loss in the absence of any retransmission or synchronization protocol.

4.3 Experimental setup

Fig. 4.4 shows the experimental setup used to characterize the proposed OCC system. In this system, the signal is transmitted in the form of fixed length packets using a beacon header. We generated a 4-bit packet in Matlab in the OOK-NRZ format. We added a single beacon header with a double amplitude compared to the high state (i.e., "1") of the OOK-NRZ signal. The electrical signal was generated using an arbitrary waveform generator (Tektronix, TTi TGA12104) for intensity modulation of the TX. This signal is fed to a driver (Newport, Model 505B) that outputs an average driving current of $\sim 180\ mA$ to an organic OLED panel (LG, LL055RS1- 64p1-OY1) with an average optical power of 0.85 W at a 1 m distance.

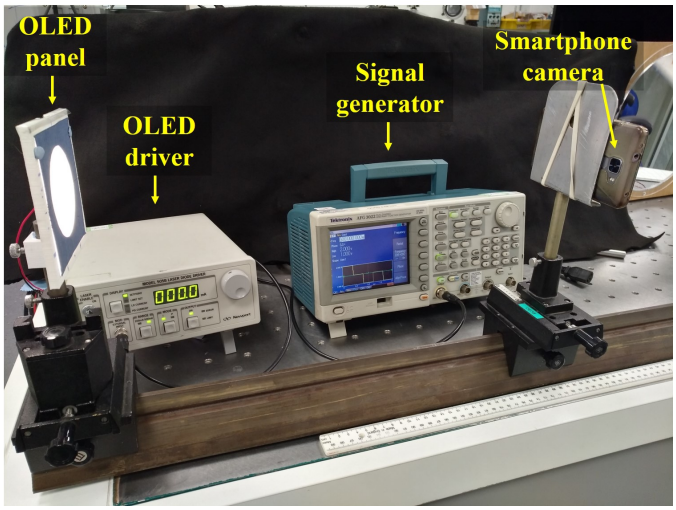

Figure 4.4: OCC system experimental setup. A Matlab code was used to generate a code fed to an arbitrary waveform generator (Tektronix, TTi TGA12104). A laser diode driver (Newport, Model 505B) was used to drive a round-framed oled panel (LG, LL055RS1- 64p1-OY1) as optical transmitter signal source. The rear camera of a smartphone (Huawei, Honor 7) was used as optical receiver, performing signal recover offline in Matlab.

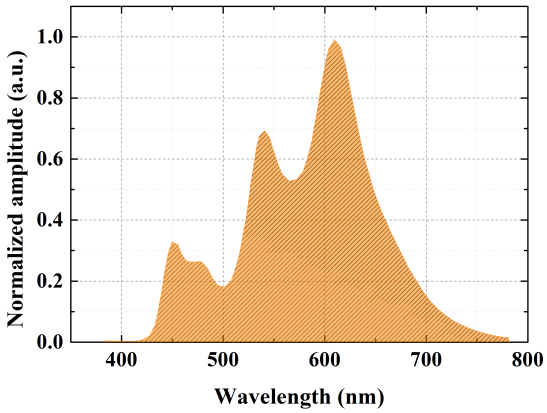

Figure 4.5: Emission optical spectrum of the employed OLED source.

At the Rx side we used a smartphone (Huawei, Honor 7) rear camera with an effective resolution of 5152×3888 pixels to take a picture of the modulated TX.
The camera was set so that the minimum of $t_{exp} = 1/6849\ s$ and an ISO of 64. Other important camera parameters were the lens focal length $f = 4.31\ mm$, and the pixel size $s_{px} = 1.12\ \mu m$ [43].
We used a Region of Interest (RoI) detection algorithm to find the TX in the picture, measure the signal source shape and use this information for signal normalization and Clock and Data Recovery (CDR).
We placed a circular aperture with a diameter of 7 cm in front of the source in order to obtain a circular image. This was done to reduce the complexity of the RoI detection algorithm, limiting the shape recognition only to round objects.

4.4 Characterization

In a similar way as the previous chapter, we performed both the electrical and optical characterization of the system. The optical spectrum emitted by the OLED employed is shown in Fig. 4.5 with a CCT of 3000K, measured by a photometer (0.5 nm resolution). The optical power emitted by the OLED panel as a function of the driving current is presented in Fig. 4.6. To acquire the system electrical bandwidth the RoI detection algorithm was used to extract the signal from the pictures of the source emitting a sinusoidal signal

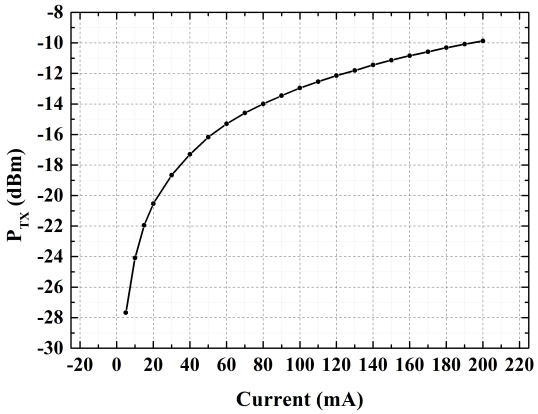

Figure 4.6: Optical power at the TX side P_{TX} vs current I curve for the OLED panel.

of known frequency. We used a Fast Fourier Transform (FFT) to perform the spectral analysis of the signal and extract the frequency response of the system to the transmitted frequency. We report the measured 3dB-bandwidth of the system in Fig. 4.7. From the figure is possible to estimate the value of the bandwidth to be approximately 4 kHz.

4.5 RoI-detection algorithm

In a real scenario the TX projection on the CIS can have any type of size and shape. A common strategy to overcome this issue is to use an algorithm to identify the Region of Interest in the picture with the source and reduce the amount of unwanted data in the frame.
We identified the prominent features of our modulated light source to distinguish the signal source from the other objects in the picture. In our setup we selected the main features of the system to be the brightness and the round shape of the source. When limited to only one of the two criteria the algorithm failed the task.

4.5.1 Intensity-based detection

In a gray-scale image of the scene, a light source represent one of the brightest objects in the frame. The algorithm used an intensity threshold value to

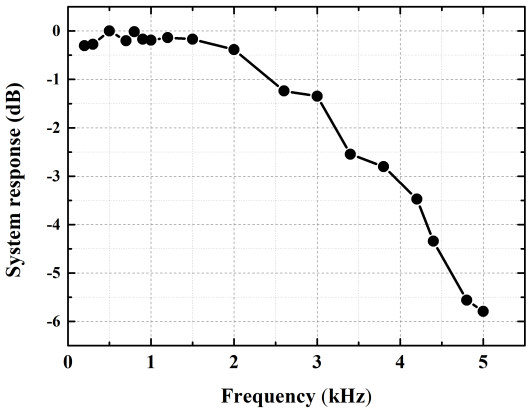

Figure 4.7: Electrical bandwidth of the OCC system, as obtained through the RoI-detection algorithm. The 3dB-bandwidth of the system it is around 4 kHz.

binarize the pixels in the picture. Compared to the threshold value the pixels were divided in two different classes: above (given intensity 1) or below (given intensity 0) the threshold value.
Among the thresholding algorithms one of the most used is the "Otsu's method" [44]. In Otsu's method a recursive algorithm is used to minimize the intra-class variance of the intensity distribution $\sigma_w^2(t)$ over the pixels, as in Eq. (4.5.1):

$$\sigma_w^2(t) = w_0(t)\sigma_0^2(t) + w_1(t)\sigma_w^2(t) \tag{4.5.1}$$

where $w_0(t)$ and $w_1(t)$ are the probabilities of the two classes (the two values of the binarized image) separated by the threshold level t. $\sigma_0^2(t)$ and $\sigma_1^2(t)$ are the variances of these two classes. The algorithm then aggregated groups of adjacent pixels with intensity value above t and used them to reconstruct separate objects. We show results of this approach in Fig. 4.8 where the sources found by the algorithm were highlighted in orange. However, Otsu's method is known to show a poor performance for non-bimodal distributions, in particular if the histogram of the pixel intensities does not exhibit a deep and sharp valley between the two peaks [45]. To highlight this limitation, is enough to place the signal source in a bright background, where the picture showed many shades of gray and the histogram had a smoother distribution. In this context the threshold calculation failed as clearly showed in where the algorithm was unable to find the source (red circle in Fig. 4.9).

(a) (b)

Figure 4.8: RoI-detection algorithm results by using Otsu's method thresholding: a)Original picture; b) Intensity-based detection of the light source using Otsu's method.

(a) (b)

Figure 4.9: Result of Otsu's thresholding for a bright background: a) Original picture; b) Picture binarized shows a threshold detection error due to bright background (orange parts).

4.5.2 Intensity and shape detection

We combined source shape recognition to calculate the optimum threshold for binarization in presence of a bright background and reject all the pixels that were not part of the source. We selected only the round shape for recognition in order to reduce the algorithm complexity in our setup.
After an experimental characterization we selected four parameters to achieve shape recognition:

1. The object must have a minimum length d_{min} of 80 pixels. We used this to ignore noisy spots or objects too far away for data extraction:

$$d_{min} > 80\ px$$

2. The ratio of pixels inside the object perimeter with intensity above the

threshold N_{above}, compared to the total number of pixel of the object N_{object} must be $> 95\%$. We forced this condition to avoid bright objects with holes due to almost round shapes (C-shaped objects):

$$\frac{N_{above}}{N_{object}} > 95\%$$

3. The difference between the geometrical area of the object A_{geom}, calculated as the product of the two half-axes of the object (the maximum vertical d_v and horizontal d_h line of pixel in the object) times π, and N_{object}, must be $< 0.1\%$. We introduced to select round object and account for tilted sources that can appear elliptical:

$$\frac{|d_v d_h \pi - N_{object}|}{d_v d_h \pi} < 0.1\%$$

4. The number of round object N_{round} that are compliant with the previous conditions must be < 10. We selected this value considering a simplified testing environment that accounts no more than 10 sources in one picture with the minimum size for data extraction:

$$N_{round} < 10$$

The algorithm started from an initial threshold value, experimentally selected to be 0.8 of the maximum intesity value (1). The software then binarized the picture and evaluated the four conditions. If one of the conditions was missing, the threshold value was lowered and the conditions were evaluated again. The algorithm kept iterating these instructions until it found at least one source or the threshold value reaches 0.
We added an image processing block to the algorithm in order to blur the picture along the rows (orthogonal to the RS effect in order to not delete the modulation). This was necessary since the presence of modulation or surface feature could introduce shape irregularities, like dark and bright bands or dots that could affect the algorithm (see Fig. 4.10). Finally, in Fig. 4.11 we report the results of the algorithm based on both intensity and shape. The picture shows the source identification in orange for images taken in presence of dark background, bright background, skewed sources, modulated sources and surface features that altered the shape of the source.

(a) Shape-recognition errors in presence of surface features

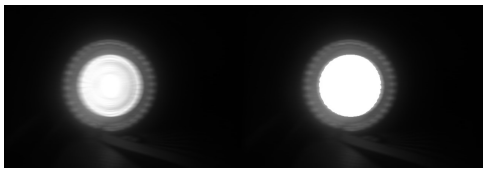

(b) Blurring effect on solving surface-dependant algorithm errors.

Figure 4.10

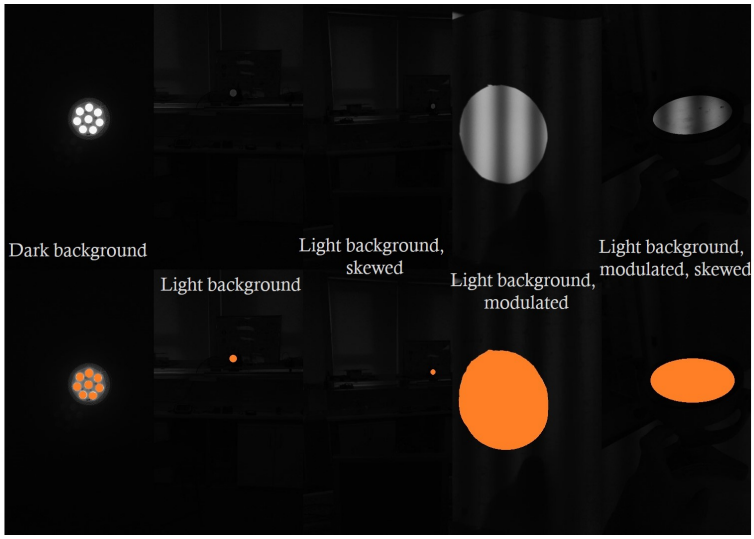

Figure 4.11: Original pictures (top) and after RoI detection (bottom) in various background and source conditions.

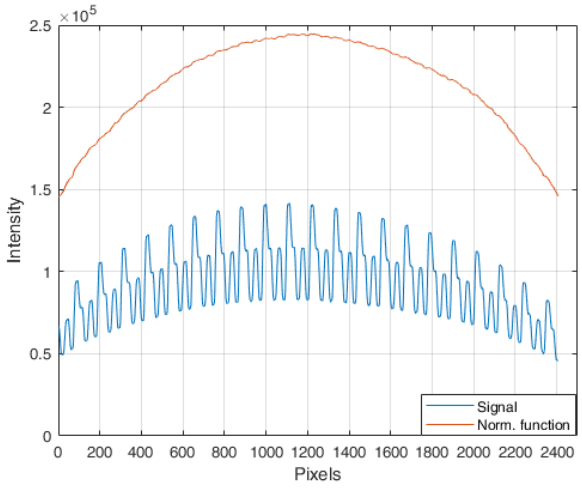

Figure 4.12: Signal extracted from a picture (blue) with the calculated normalization function (red). The link span was 10 cm with a transmission rate of 3 $kbit/s$.

4.6 Applications of the detected RoI

We used the RoI detection algorithm to detect and measure the signal source. We exploited this information to address the distortion caused by source shape and the information loss with the RS-OCC systems with distance.

4.6.1 RoI-based signal normalization

In this section we present the use of the RoI detection algorithm to normalize the signal extracted and reduce the impact of the source shape on the signal envelope. The algorithm identified the source in the image and cropped the smallest rectangular area around the captured picture. The algorithm created a binary image by setting all the RoI pixels to intensity 1 and all the other pixels to 0. From the binary image the software calculated a normalization function using the source profile by summing along each row of the binary RoI image. We extracted the signal by summing the pixels' intensities along each row and divided the value obtained by the normalization function to remove the shape-induced distortion.
In Fig. 4.12 we report the extracted signal (in blue) and the normalization function (in red), with a transmission rate of 3 $kbit/s$ and a packet structure of [21010]. Fig. 4.13 shows the original picture of the TX taken by

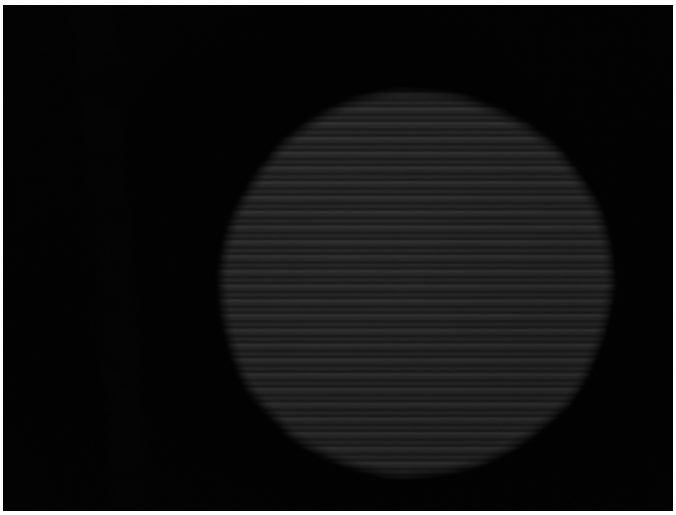

Figure 4.13: Original picture of the modulated source at 10 cm with a transmission rate of 3 $kbit/s$.

the camera at 10 cm distance. The round shaped OLED affected the signal intensity introducing a circular envelope and dimming its values from the center to the edges of the profile. The normalization function followed the same behavior with a slightly different curvature.
The impact of the normalization became even more evident when shown on eye diagrams, as in Fig. 4.14. It can be easily seen a notable eye opening at two testing distances of 10 cm, a) to b), and 100 cm, c) to d). The results are more evident at short distances due to a higher number of samples. Finally, we designed a dedicated CDR strategy, which is robust to the additional signal distortion induced by the pixels blooming effect of RS-OCC.
We used a double-threshold Otsu's method to classify the pixels in three bins of intensities: 0, 1 and 2. The symbols with intensity 2 were identified as beacons. We divided the measured distance in pixels between the beacons of the first and second detected packets by the packet length in bits, fixed in this setup, to recover the received bit time length in pixels.
We removed the beacon headers and sampled the signal at the center of the bit, compared them with an optimal threshold level for bit detection.

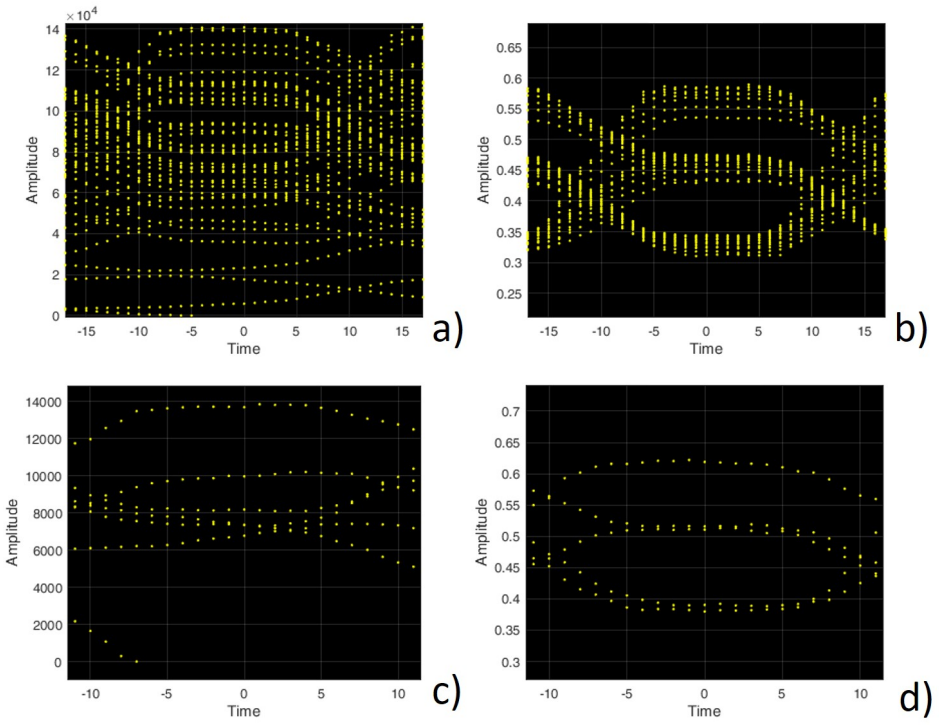

Figure 4.14: Eye diagrams of the received signal at 3 $kbit/s$: (a) original signal at 10 cm, (b) normalized signal at 10 cm, (c) original signal at 100 cm, and (d) normalized signal at 100 cm

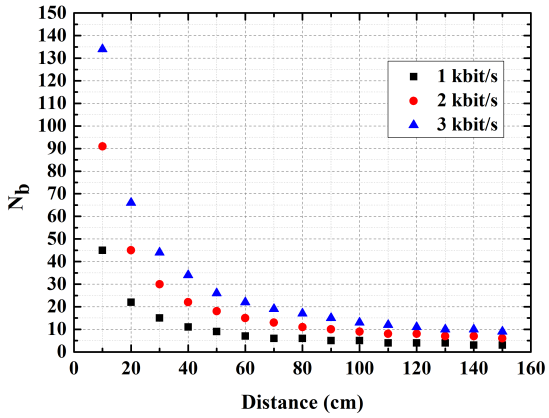

Figure 4.15: Received bits as a function of distance for 1 $kbit/s$, 2 $kbit/s$ and 3 $kbit/s$ transmissions

4.6.2 Packet repetition schemes for distance-related information loss

To outline the relationship between the number of bits received from a single image and the link span we performed a set of measurement on the number of received bits as a function of distance for three different transmission rates, 1 $kbit/s$, 2 $kbit/s$ and 3 $kbit/s$. The results are presented in Fig. 4.15, where $N_b = N_{samples} \cdot N_{spb}$ was the number of bits extracted from a single picture. The reported data shown an exponential decrease of N_b with the distance, displaying a bigger impact on higher transmission rates. This was true in particular for shorter distances, becoming less and less important as the link span increased. This was clear when confronted with Eq. (4.2.6), where N_{spb} was directly proportional to the bit time t_b at fixed t_{RO}. To address the throughput reduction with distance, we simulated the effect of the transmission of multiple copy of the same packet to avoid information losses. The knowledge of the source projection size was used to tune the system in order to avoid the loss. Two options of a double packet (2-packet) and a cyclic packet (C-packet) repetition were adopted (see Fig. 4.16). In the first option, a minimum of 2 packets should be visible in the source projection on CIS for CDR as explained in Section 4.5.1. In the second option the Beacon Jointed Packet Reconstruction (BJPR) was used as described in [38], where beacon headers were adopted to cut-and-paste out of synchronization packets, modelling the data stream as a cyclic sequence. The results of

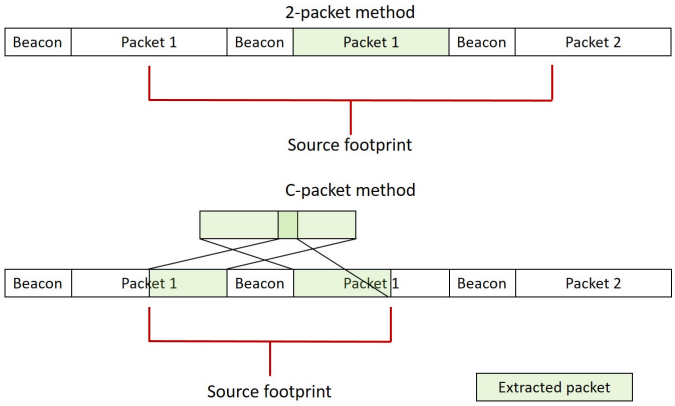

Figure 4.16: Repeated packet methods to avoid information loss in bursty channel with no synchronization: in 2-packet method, a minimum of 2 packets should be visible in the source projection for CDR; C-packet method uses beacon headers to cut-and-paste out of synchronization packets, modelling the data stream as a cyclic sequence.

the simulation are reported in Fig. 4.17. It can be clearly seen that the 2-packet repetition showed the worse performance compared to the other methods for a transmission span up to $90cm$. However, note that, with no repetition the throughput reduction meant a loss of information. Instead, 2-packet and C-packet methods present no packet losses related to the out of projection pixels, with the second method that showed the same throughput performances of the no repetition scheme.

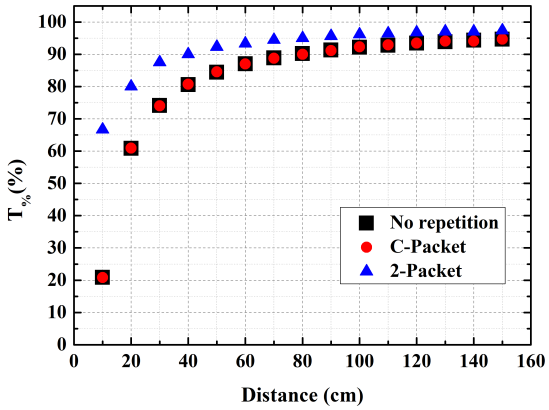

Figure 4.17: Throughput loss as a function of distance, with no repeated packet, 2-packet or C-packet methods.

Chapter 5

Underwater Optical Wireless Communications

In this chapter I present the results of the OptoCOMM sub-project in the framework of SUNRISE European project. The author participated actively in the project in the simulation and test, both in laboratory and at sea, of a novel pair of modems for Underwater Optical Wireless Communications (UOWCs). The author contribution was limited to the optical layer of the modem and has not participated in the design of the electrical part or in the realization of the watertight containers.

5.1 State of the art

The rising number of human underwater activities increases the need for efficient systems and devices deputed at sea-monitoring, ranging from buoys, ships,Underwater Wireless Sensor Networks (UWSNs), Remotely Operated Vehicles (ROVs) and Autonomous Underwater Vehicles (AUVs) [46]. Unmanned underwater vehicles are today a mature technology, which is stimulating also the research towards multi-vehicles coordinated operation [47] [48] [49]. A key task of these vehicles is to record and transmit data to a central unit, e.g. staff on a ship, in particular high-resolution images, and videos. Transferring this type of data timely requires high bit-rate transmission. Vehicles are sometimes forced to use wired solutions, which have limited applications, since they impact on device mobility and reconfigurability [50]. Due to the strong attenuation of RF in water [51] [52] [53] [54], today the applications requiring vehicle mobility mostly rely on acoustic modems [55]. Although low-frequency waves can travel over long distances [56], high-

frequency acoustic waves suffer from strong absorption and mechanical limitations, which make them unsuitable. Therefore the available bandwidth of common acoustic modems is around few kHz which strongly limits the maximum bit-rate [57]: high-end acoustic modems can have a transmission rate up to 35 $kbit/s$ [58]. Furthermore underwater acoustic transmission is strongly affected by noise, generated by different sources. In order to provide for both high-speed and wireless operation, Underwater Optical Wireless Communications (UOWCs) is an attractive alternative, which is rapidly gaining momentum.

UOWC systems were proposed based on LDs or LEDs. LDs have wider bandwidth and higher optical power but suffer from misalignment, and are more expensive compared to LEDs. First UOWC results were taken using LDs [59], [60]. Recently LEDs were also considered in [61] and, depending on bit rate and water attenuation, this technology can reach $Mbit/s$ rates over distances of tens of meters [62] [63] [64] [65]. All these remarkable results, however suffer from the strong limitations that can have a key role when considering practical implementations: the channel has almost ideal transmission with very low attenuation, the transmission distance is short ($< 10\ m$), there is no relevant external noise sources (e.g., sunlight). Mostly, in the papers cited above, UOWC systems were working on dry setups, being both the TX and the RX outside the water, hence with no the need for waterproof packaging. Furthermore the channel was the clean and still water of an indoor pool, thus having no turbidity, no relevant turbulence and controlled background illumination.

An operational environment with such conditions is that of commercial and military harbors, where AUV-based patrolling and surveying is actively developed [66], with the constraint of not resurfacing in order not to interfere with normal harbour operations. In recent years, our group used blue LEDs and DMT modulation to demonstrate 58 Mb/s transmission at 2.5 m distance in clear water. The setup was tested using an outdoor pool with a waterproof TX and a RX, both submerged [67]. The system worked under strong sunlight illumination, which poses a severe limitation to the achievable Optical Signal-to-Noise Ratio (OSNR).

Building on this preliminary result, we designed and tested of a novel optical communication system, oriented, but not restricted, to operations in daylight harbor conditions, i.e., in presence of both high sunlight disturbance and high water-turbidity. The system was realized in the framework of the EU-FP7 SUNRISE project [68] and it is thus suitable for integration in the project network of underwater things as part of the Littoral Ocean Observatory Network (LOON). The realization of the optical modems has

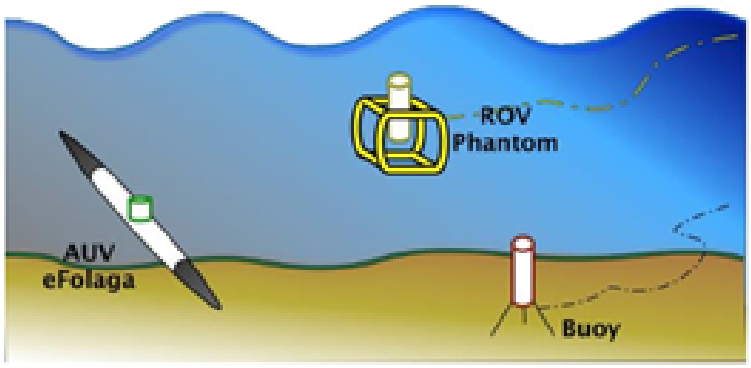

Figure 5.1: The application scenario, where one optical modem is equipped on the eFolaga AUV, one battery powered in the ROV and one connected to LOON infrastructure.

been achieved with the collaboration of Integrated Systems for the Marine Environment (ISME), that realized the software part and the watertight containers. The results reported here show that the UOWC modems provide a reliable 10Base-T IEEE standard bi-directional transmission (10 $Mbit/s$ Ethernet) up to 10 m in very shallow harbor water and daylight condition. On the application layer side, the system is also fully integrated with the SUNSET software framework of the SUNRISE project, allowing the operation and data transmission both from local and remotely connected working stations (as shown in Fig. 5.1). In [69], [70] and [71], we reported the preliminary results of the early stage of the OptoCOMM development, particularly dealing with testing of the optical part. While the final design and field-testing are reported in [72] and [73].

5.2 Underwater channel characteristics

5.2.1 Water attenuation

electromagnetic (E.M.) waves are a faster communication media compared to acoustic waves, however RF transmissions are strongly attenuated in water mainly due to absorption and scattering phenomena. Fig. 5.2 shows the water attenuation coefficient as a function of λ for E.M. waves [74].
The impact of transmission medium on a signal of power P_{TX} gives a received signal power P_{RX} as in Eq. (5.2.1) derived by Eq. (2.4.9) in Sec-

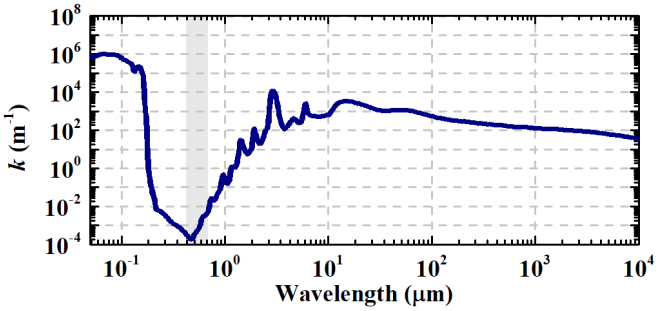

Figure 5.2: Water attenuation coefficient for electromagnetic radiation as a function of its wavelength. Visible light range is highlighted by the gray area.

tion 2.4:

$$P_{RX}(d) = \frac{P_{TX}}{d^2} e^{-kd} \tag{5.2.1}$$

Where d is the distance and

$$k(\lambda) = a(\lambda) + b(\lambda) \tag{5.2.2}$$

with $a(\lambda)$ and $b(\lambda)$ being the absorption and the scattering coefficients of the medium, respectively.
The two phenomena describe the interaction of between the photons and the medium: the absorption is due to both inorganic and organic substances in water [58]; scattering, resulting in the deflection of the E.M. waves from the original direction, leading to an intensity reduction of the signal.
As example, an attenuation coefficient k of 10 m^{-1} introduces an attenuation of 43 dB after just 1 m transmission distance. It can be clearly seen that in the visible region (the gray area of Fig. 5.2) there is a minimum of attenuation, around the blue wavelength ($\sim$ 470 nm). However, as already said, absorption and scattering are phenomena dependent on the nature of the substances present in the water. Hence, as expressed by Table 5.1, different water conditions lead to different coefficients, in particular the attenuation minimum is red-shifted in more turbid waters (see Fig. 5.3).
Using Eq. (5.2.1) we can simulate the expected channel attenuation as a function of the distance d. Since our system was based on a LED transmitter we assumed a Lambertian source (see Section 2.2.2) and computed the simulation in Fig. 5.4 at different values of k.

Water type	a(m^{-1})	b(m^{-1})	k(m^{-1})
Pure sea water	0.040	0.002	0.043
Clear ocean water	0.114	0.037	0.151
Coastal ocean water	0.179	0.219	0.399
Turbid coastal water	n.a.	n.a.	0.8

Table 5.1: Absorption (a), scattering (b) and attenuation (k) coefficients for different type of waters [58] [62].

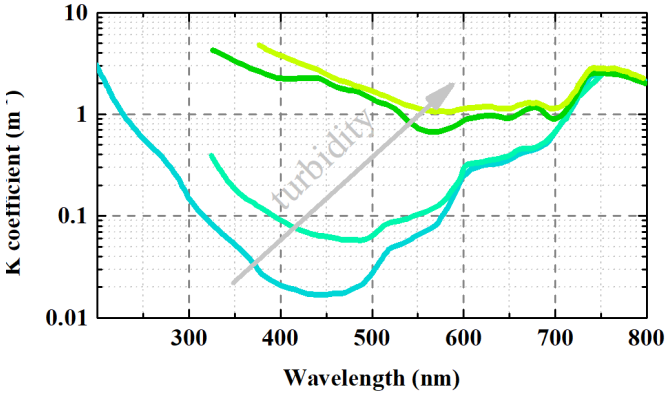

Figure 5.3: Water attenuation coefficient for the visible spectrum at different values of turbidity.

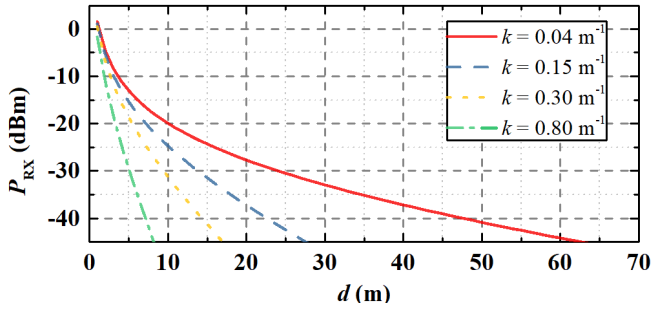

Figure 5.4: Simulated received power P_{RX} as a function of distance d for different attenuation coefficients k.

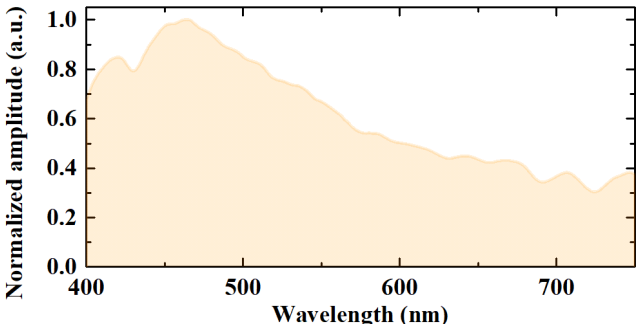

Figure 5.5: Measured solar spectrum at sea level during a field test.

5.2.2 Sunlight background

In Chapter 2 and Chapter 3 we have already highlighted the impact of Background (BG) light on VLC.
Especially in shallow waters, the BG light (sunlight) can have high values: in the first tests, we measured around 4.5 dBm on the pier, due to sunlight. This is a relevant value, which, even assuming the use of an optical filter at the RX, produces a photo-current that can be comparable with the signal current limiting the performance of UOWC links.
In Fig. 5.5 we report the solar spectrum of a sunny Italian summer day. It was measured during the field test of our system with a photometer (0.5 nm resolution), placed just above the water surface pointing horizontally. It is clear that even the sunlight is affected by the water attenuation, changing its impact with the working depth: as known, deep ocean is by far less lighted then shallow harbor waters. However, in order to have modems capable of working in all conditions (shallow/deep waters, day/night, etc.), the impairments due to sunlight in UOWC cannot be simply neglected and they must be carefully taken into account when designing the optical communication system.

5.3 Optical modems design

In this section, we describe the key elements of our final UOWC modems: we present a general description of the modems as a whole, with the optical communication part, the electronic (and software) design and the watertight containers (see Fig. 5.6).

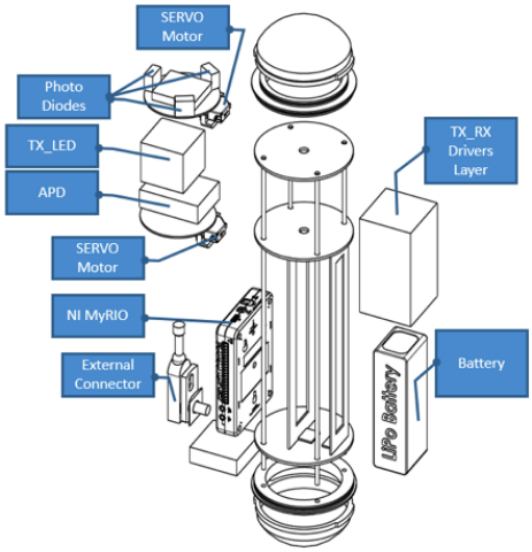

Figure 5.6: Original design of the optical modems

5.3.1 Optical Communication part

The optical communication part had three sections: TX, RX and the monitoring part (see Fig. 5.7a). The parts were assembled in three consecutive transverse sections of a cylindrical support (see Fig. 5.7b). The TX was made by a LED array with the emission peak at 470 nm, 20 nm optical bandwidth. We chose the LED array instead of other light sources (e.g. lasers), due to their reduced cost and small temperature dependence. Blue light was chosen to obtain the minimum attenuation in clean water; although the modems are first meant to prove shallow water transmission, the main operative scenario in future will be deep clear waters.
The LED chips were connected in series and biased at 21 V (around 400 mA), giving a total luminous flux of $\sim$ 300 lm (from datasheet). The signal from the Ethernet interface (Manchester-coded signal with 10 $Mbit/s$ data rate [75]), after an amplification stage (Amp_{TX}, 25 dB gain, 130 MHz 3dB-bandwidth), was superimposed to the DC bias voltage of the LED by means of a bias-tee. We used a low-cost plastic lens at TX to further shape the beam, increasing the optical power density at the receiver. The lens reduced the Lambertian pattern of the LED beam down to 20 degrees in air. In the aligned condition, this lens gives an optical gain of $\sim$ 11 dB. The RX encompasses an APD module with an integrated Trans-Impedance

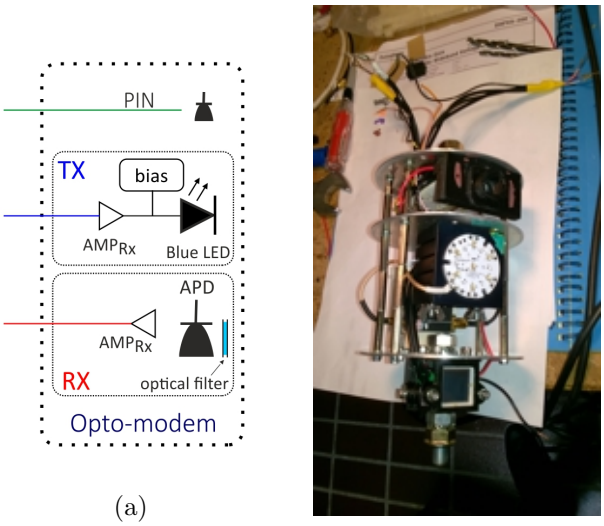

(a) (b)

Figure 5.7: Optical communication layer: a) scheme; b) picture

Amplifier (TIA) having an active area of 100 mm^2 and a frequency cut-off of 11 MHz.
As already said in the previous section and in Chapter 2 background light can severely impact VLC system operation, in particular in outdoor environment. It is important, then, to take care of this factor in the design of the optical layer of the modems.
The ambient light received by the photo-detector P_{BG} can be factorized with several parameters, given by this expression:

$$P_{BG} = A_{RX}(\pi FOV)^2 T(\Delta\lambda) L_{SUN}(\lambda) \tag{5.3.1}$$

where A_{RX} is the active area of the receiver, FOV is the Field-of-View of the RX, $T(\lambda)$ and $\Delta\lambda$ are the optical band-pass transmittance and the bandwidth of the RX filter, and L_{SUN} the solar radiance at the same wavelength window. In order to minimize the effect of background light, we acted on some of these parameters in the design of the optical part: active area, FOV and characteristics of the filter in front of the APD. Then, we conveniently used a blue filter to reject most of the ambient light. Whilst the center wavelength of the filter was an obvious choice to match the LED peak wavelength, the bandwidth of the filter was chosen to maximize the signal to background power ratio.
We tested two different blue filters. The first filter had a bandwidth of

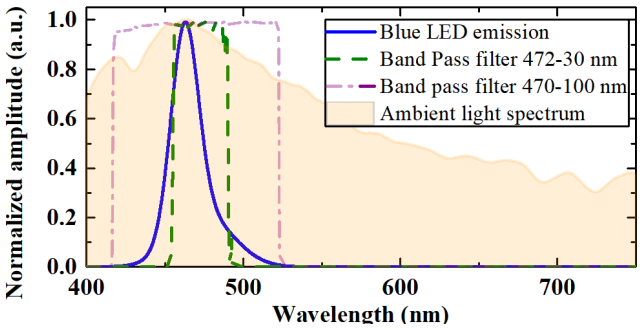

Figure 5.8: Optical spectra in the visible range. In the graph we report the spectra of emission of the blue LED used and of the solar emission measured at sea level during the field test. Transmission spectra of two different optical filters implemented in preliminary (purple, dot-dashed) and final (green, dashed) tests are also reported superimposed to highlight the transmission spectral window.

100 nm, which covered all the emission spectrum of the TX, while the second filter had a 3dB-bandwidth of 30 nm, comparable with the LED emission (20 nm), hence cutting out the tails of the emission. The spectrum of the LED is shown in Fig. 5.8 with the transmittance shape of the two filters. In the same figure, we report also the background spectrum measured by a photometer (0.5 nm resolution), placed just above the water surface, pointing horizontally. The spectrum was taken at sea-trials around noon, in a sunny day in July.
Although the 30 nm filter slightly reduced the optical power from the LED by 1 dB, it rejected a much greater portion of the background light. Considering normalized amplitudes, the gain in OSNR with the narrower filter was around 3 dB.
Another feature of the background sunlight is its directionality: sunlight could reach the RX directly or because of Rayleigh scattering both in the atmosphere and in water. Our source is positioned horizontally, in front of the receiver. It can then be seen that reducing the FOV of the RX in our condition preserves the signal optical power at the receiver but can strongly limit the impact of the incident background noise. This is of course not a general statement: if the modem is operated in a dark environment, a wider FOV can allow to collect some more signals and could be beneficial. In our case, we shrunk the FOV by a mechanical frame mounted in front of the APD. Common FOV for a planar receiver is around 180 degrees (2θ angle),

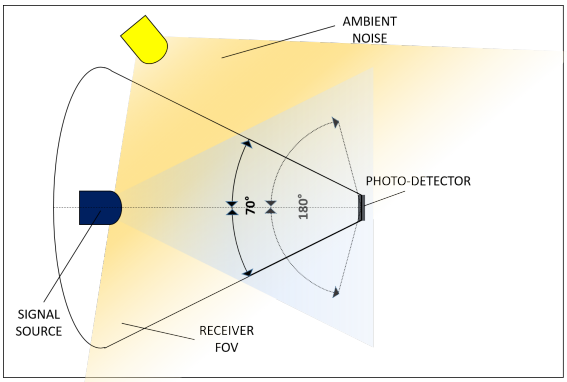

Figure 5.9: Schematic representation of the geometrical impact of the reduction of the FOV at the RX in presence of a directional source of ambient light.

and our frame reduces this angle down to 70 degrees (see Fig. 5.9). We also measured that the entire sunlight spectrum corresponds to around 4.5 dBm at noon. From this value, we estimated a received background optical power (P_{BG}) of about -6 dBm, considering the active area of the photodetector, the effect of the optical filter, the water attenuation, and the FOV reduction of the photo-detector.
The output of the APD was then properly amplified by a variable voltage amplifier (10 to 40 dB gain). This amplifier (Amp_{RX}) was needed to produce a signal with the electrical amplitude compliant with Ethernet interface standards. Finally, a monitoring layer was added to the previous ones, with one cheap PIN; this solution allows to detect and measure the amount of light present at the RX.
We highlight that all used devices are commercially available and have limited cost, which could make the final prototypes suitable to be massively deployed over several AUVs.

5.3.2 Electronic layer

OptoCOMM project did not include the realization of mobile to mobile transmission with the need for coarse alignment and handshake protocols. However, as part of the design of the electronic layer, two servo motors were included to allow the optical communication part to move independently.

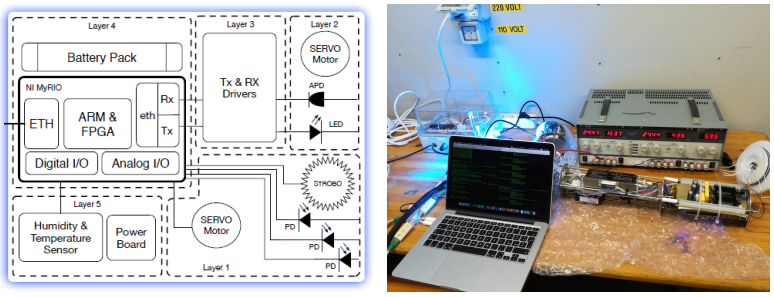

(a) (b)

Figure 5.10: Electronic layer structure: a) original scheme; b) practical realization

The electronic layer was initially more complex, including 5 different sublayers (see Fig. 5.10). Layer 1 was initially composed of three different PINs to initiate handshaking protocols between modems. Later we incorporated this layer in the optical communication part, removing everything but one PIN to be used as optical power monitor. Layer 2 contained the LED and APD of the optical communication layer. We positioned all the required biasing and amplifying stages in layer 3 (see Section 5.4.1 and Section 5.5.2 for more details). The on-board modem electronics included ancillary sensors (e.g., humidity and temperature) (Layer 5), power (Lithium Polymer battery), and an FPGA-based Application Real-time Microcontroller board (ARM/FPGA) for firmware/software installation and overall modem control and management (Layer 4). We selected as ARM/FPGA the National Instrument (NI) myRIO, composed by an ARM Cortex A9 processor and a Xilinx FPGA, including the NI Linux Real Time Operating Systems, analog and digital connections, and Ethernet ports. In addition, the electronics included several DC/DC converters, with appropriate analog filtering and insulation to avoid power cross-talk on both data and power lines. The software developed on the myRIO managed the commands received from a user and sent files through the optical layer. Moreover, to integrate the UOWC modems in the SUNRISE networking structure, we realized the modem interface compliant with the SUNSET Software Defined Communication Stack (SDCS) [73] [76].

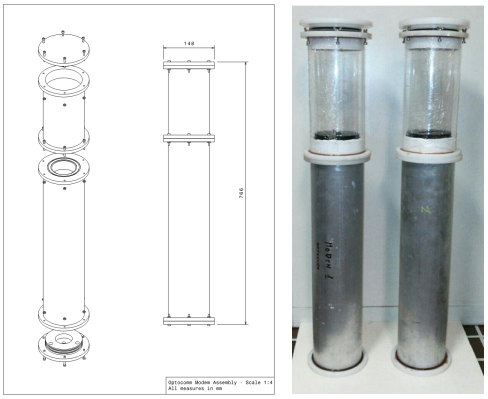

(a) (b)

Figure 5.11: Watertight containers: a) original scheme; b) practical realization

5.3.3 Watertight containers

The modems pressure hull was designed and realized as composed by an assembly of two parts (Fig. 5.11): the body (containing power and Ethernet signal boards) and the head (containing the optical layer as described above). Both parts were composed by a cylindrical tube, enclosed between two acetal neck flanges. While the body tube is made from a 6xxx-series anticorodal aluminum alloy, the head case is made from Perspex. Both tubes were bonded to the corresponding flange necks using a special sealing adhesive, commonly used in marine applications. The upper flange of the head was closed by an acetal blind flange constrained by six bolted screws. In order to prevent any water leakage, a double radial o-ring seal was realized between the blind flanges and the corresponding internal surfaces of the necks. The o-ring glands were designed and manufactured according to the guidelines provided by common seal manuals and handbook. In order to verify the possibility to employ the pressure hulls during a mission, the parts were tested in a custom pressure chamber available at the CMRE facility, La Spezia. The head, being a $3 - mm$ wall tube and made from Perspex, was tested to reach 50 m depth maintaining its full integrity and the required watertight properties. Failure depth for the head pressure hull was measured at about 60 m depth.

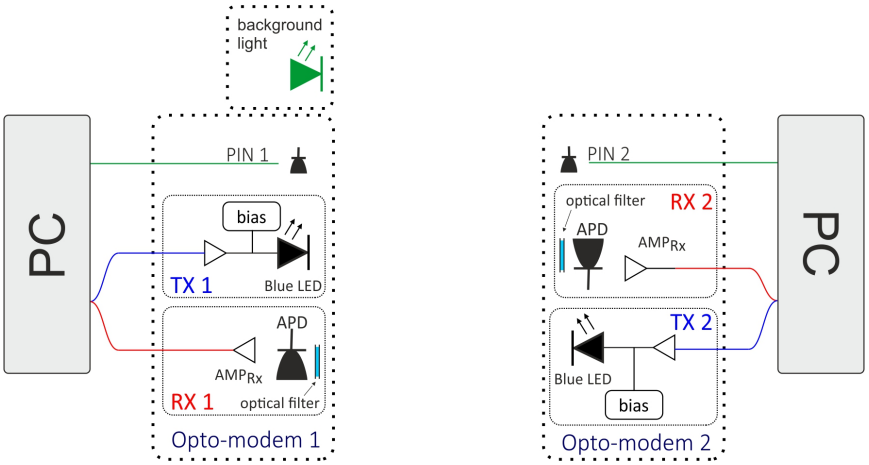

(a)

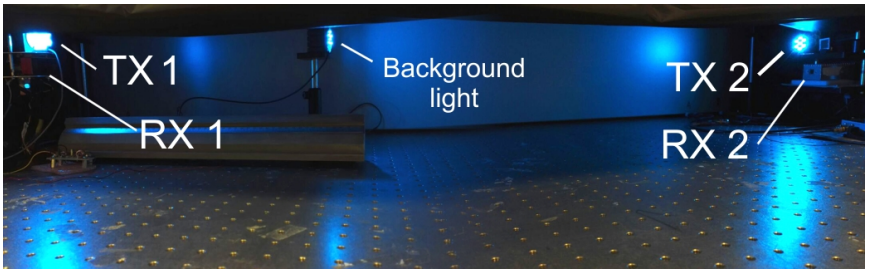

(b)

Figure 5.12

Figure 5.13: Lab experimental setup: a) scheme; b) picture

5.4 Laboratory tests

Before the sea-trials experiments, we performed a wide number of tests in the lab, spanning the various issues of the optical modems. The main issue of the UOWC system was the presence of strong background light. During these preliminary tests we focused mainly on characterizing the impact of background light on the system.

5.4.1 Experimental setup

For this analysis, we realized the experimental setup shown in Fig. 5.12. TX and RX were placed in D-LOS configuration and covered with a black screen, blocking light from all external optical sources. A controlled back-

ground light was then emulated by a secondary unmodulated blue LED source (with the same wavelength used for the TX). Thus, all the produced noise was in the transmittance band of the optical filter. The optical power of the signal was controlled by optical attenuators placed in front of the TX. With this setup, we were able to simulate various environmental conditions, such as different transmission distances and different levels of ambient light, performing transmission measurements with different OSNR. To test the system, we connected the modems to the Ethernet interfaces of two PCs. We then used a software to generate and send random data packets measuring the packet loss at the RX.
We stress that, given the design constrains due to the final Ethernet implementation, common bit error rate measurements cannot be carried out in this case, thus only packet loss values can be reported. For this test bench, all the devices were powered by lab power supplies. The received optical powers (both signal and background) were measured with a PIN placed next to the APD and re-scaled to take into account the different active areas and responsivity.

5.4.2 Analysis of the background light impact

We first characterized the impact of the unmodulated light on the RX performance due to saturation, which is induced by both signal and background light on the receiver module (APD and TIA). To this aim, we set a given value of the TX optical power (P_{RX}) and modulated the TX LED with a 1 MHz sine-wave. Then, we measured the amplitude of the RX output signal (V_{RX}), as a function of the intensity of the ambient light P_{BG} (by changing the bias current of the unmodulated LED). The measurements were repeated at different P_{RX} values. The experimental results are shown in Fig. 5.14. Here, we report the V_{RX} values as a function of the total received power ($P_{tot} = P_{RX} + P_{BG}$). The values of P_{tot} naturally started from around P_{RX} (i.e., P_{BG} negligible) for each curve. As expected V_{RX} is higher with higher P_{RX} , while, increasing P_{BG} , V_{RX} remains constant until the total received power reaches -17.5 dBm (highlighted in the figure with the vertical dashed gray line). Above this value, any further increase of P_{BG} reduces the signal amplitude at the RX output. We highlight that this was the most common working condition of the harbour, because the received ambient light under the water surface was around -6 dBm. From the previous results, we have to expect a significant increase of RX sensitivity in the usual operating conditions, from the values observed in the dark. It was thus needed to characterize the UOWC system before the sea field tests, by

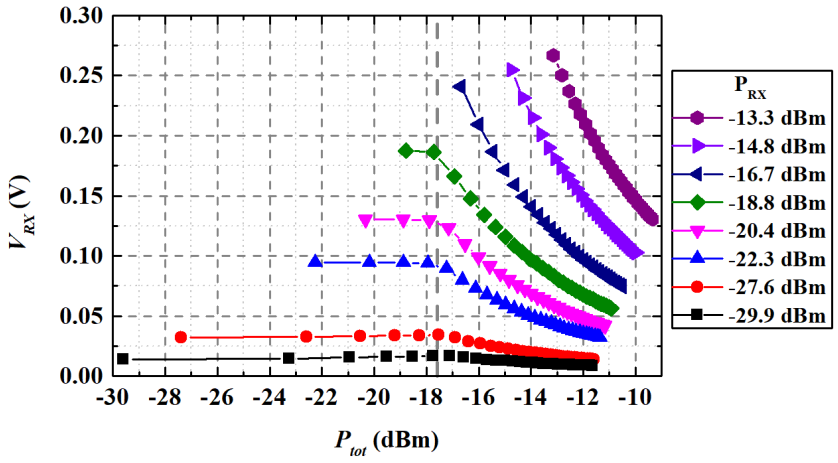

Figure 5.14: V_{RX} as a function of the received optical power P_{tot} (signal plus background light). The curves are taken at different P_{RX} indicated on top. The vertical dashed line indicates the threshold, above which V_{RX} reduces.

measuring the impact of the background on the system performance. We sent 600000 Ethernet packets to the TX and measured the packet loss at the RX output as function of the received signal power. We present these results in Fig. 5.15. Here the different curves were obtained for different values of background light (represented in different colors). The considered background intensities range from dark condition ($-50\ dBm$), to our typical average sunlight ($-6\ dBm$). As can be seen, we have a step-like behavior in the packet loss measurements. This is mainly due threshold behaviour of the Ethernet interface, causing packet loss even when the quality of the signal was still good. As example of signal degradation, we report in Fig. 5.16 various eye diagrams taken varying P_{RX} from -28 to $-34.5\ dBm$, at a fixed background light ($P_{BG} = -19\ dBm$). We outline that these eye diagrams are typical of the Manchester-coded signal (IEEE 802.3), where at the center of the bit there is always a transition (i.e., in our AC-coupled case, the waveform crossed the zero axis). These eye diagrams represent four significant cases. The first eye diagram was taken with the system in an optimal condition ($P_{RX} = -28\ dBm$, no packet loss); the second eye diagram was taken at lower power ($P_{RX} = -32 dBm$), and still error-free; the third one, taken at just 1 dB lower power ($P_{RX} = -33\ dBm$) was observed with some non-negligible packet loss ($< 1\%$). Finally the last eye was taken

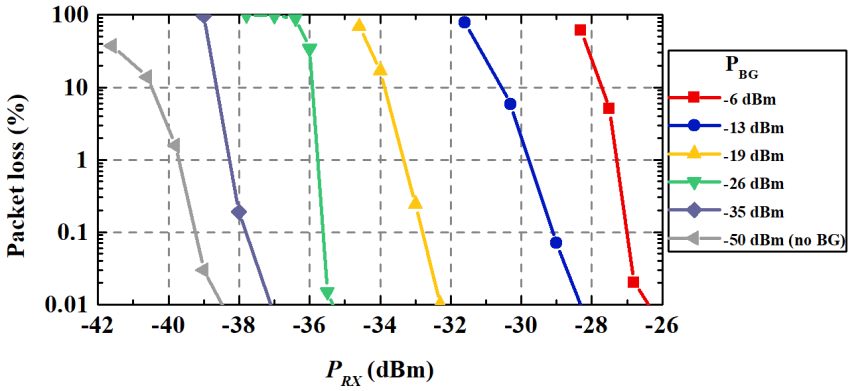

Figure 5.15: Packet loss measurements as a function of the signal power P_{RX}. The measurements were taken with different P_{BG} values reported on top.

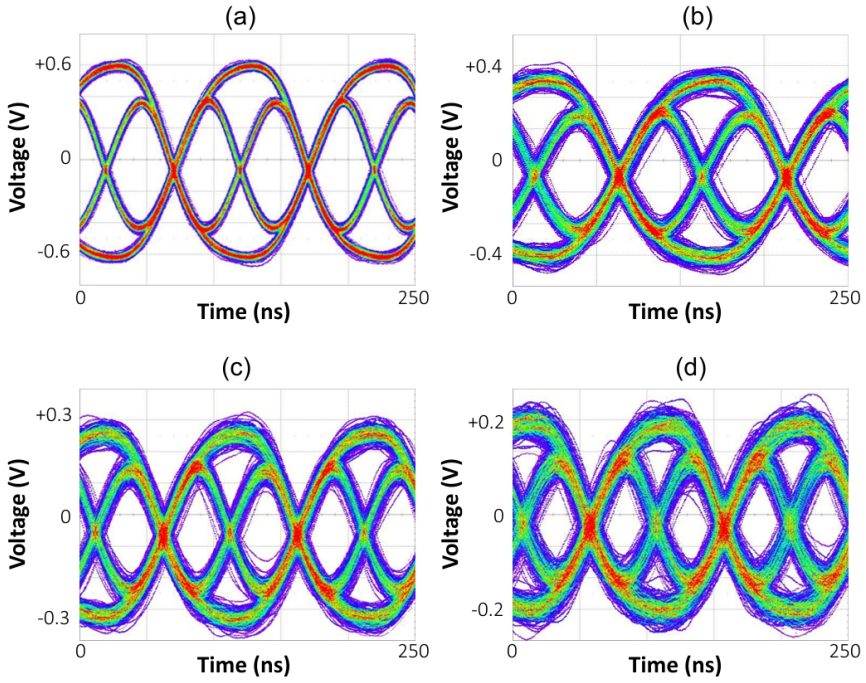

Figure 5.16: Eye Diagrams taken with $P_{BG} = -19\ dBm$ and at different P_{RX} : $-28\ dBm$ (a); $-32\ dBm$ (b); $-33\ dBm$ (c); $-34.5\ dBm$ (d).

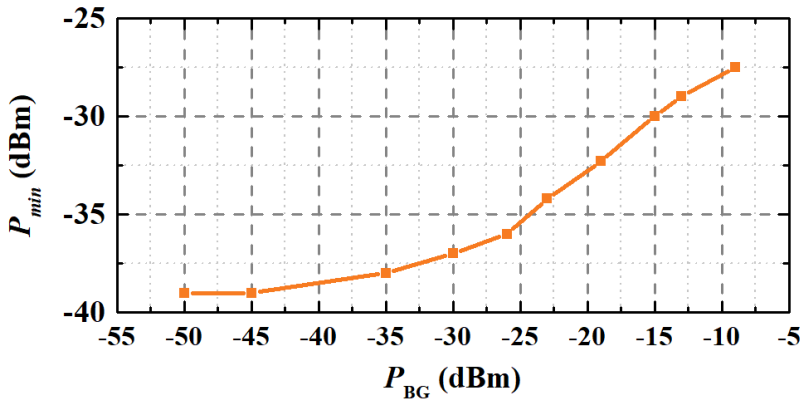

Figure 5.17: Signal optical power required to guarantee a transmission in error-free condition for specific value of background light.

at $P_{RX} = -34.5\ dBm$, when the packet loss was greater than 60%. In all cases, we observe clearly a threshold-like behavior, where for any P_{BG} value we can find a minimum required power P_{min} to correctly operate the system. From the data showed in Fig. 5.15, we extrapolated the P_{min} values for any specific value of ambient light P_{BG}. This curve is reported in Fig. 5.17. As can be seen, there is no linear relation between the P_{min} and P_{BG}, keeping in mind also the saturation effect on the APD at high optical power. These data give a quantitative means to predict the behavior of the system under moderate and strong illumination condition. As example, after this characterization of the optical modems, we expect that our UOWC system can work even with strong ambient light of 4.5 dBm/cm^2 (sunny day in summer) when received signal power P_{RX} is at least $-26\ dBm$. Depending on the water turbidity, different transmission distances can be achieved. For example, considering a $k = 0.25\ m^{-1}$, a distance of 8 m can be achieved (see Fig. 5.4). Considering a dark environment, an estimated distance of 13 m can be achieved with same condition of water turbidity.

5.5 Field test

5.5.1 Environmental conditions

As final demonstration, we performed various sea-trials to test the system performance in a real sea environment. The trials were conducted at the

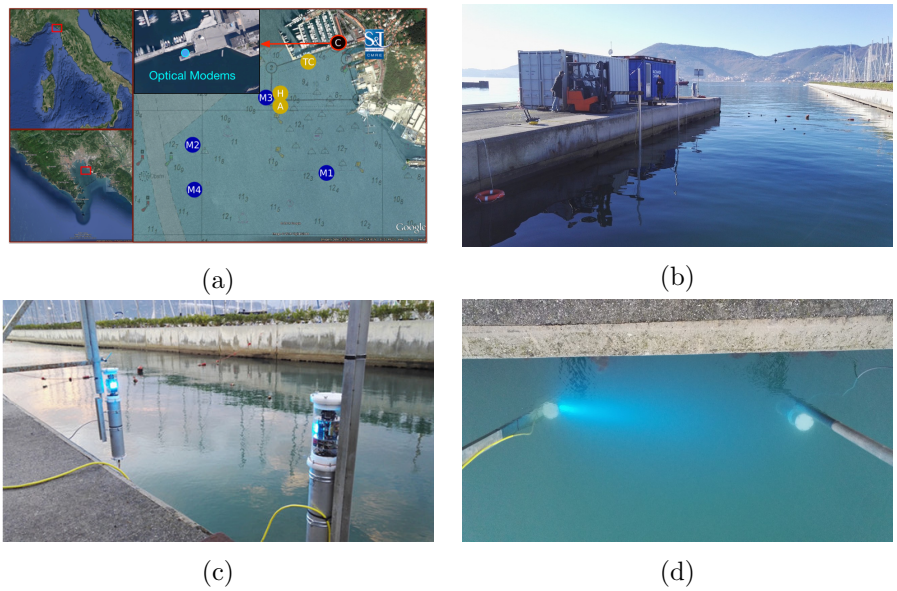

Figure 5.18: Pictures taken during the field test at sea: a) map and satellite view of the testing site; b) experimental basecamp container on the harbour pier; c) modems before submersion at $d = 2.5\ m$; d) optical transmission between submerged modems

harbor of La Spezia (Italy) Fig. 5.18a. The experimental area is located in the middle of two piers and only open to research activities Fig. 5.18b. We could access a pier, where the modems could be submerged and, at the same time, we could keep both connected by cables (see Fig. 5.18c and Fig. 5.18d) the connection allowed us to control the modems, to send/receive data and to measure the transmission performance using the monitoring equipment in a container on the pier. Here, the water turbidity is much higher than in an open sea. We report in Fig. 5.19 the measured optical values as a function of the distance d between the modems, in a single specific day for consistency (k coefficient is expected to change randomly, even in the same location). Due to time constrain for the trial, we decided to take measurements only at distances useful for the communication point of view. In this figure we also show the fitting curve based on Eq. (5.2.1). The fitting gives us a $P_{TX} = 1.15\ mW$ and $k = 0.25\ m^{-1}$. The P_{RX} value shows excellent agreement with the values taken in laboratory (see Section 5.4.2) at 1 m free-space (1.2 mW), confirming the goodness of the fit. During the experiment, we measured the turbidity by means of a turbidimeter (Ocean Seven 305

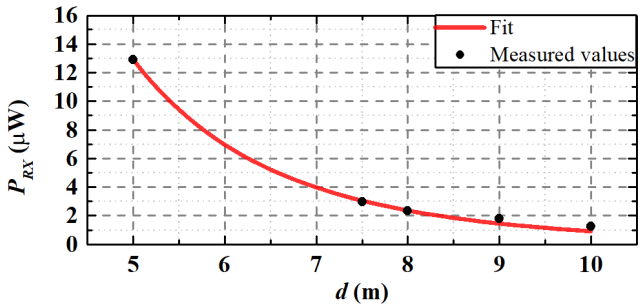

Figure 5.19: Measured received optical power P_{RX} at different distance d between the modems. The fitting curve is based on the theoretical expression of the propagation of a Lambertian pattern of Eq. (5.2.1).

Plus by Idronaut), in terms of Formazin Turbidity Unit (FTU). The value was found in the range between 1 and 1.5 FTU: from this we can obtain another estimation of the k coefficient, as it was previously reported that k and FTU values are related by a linear relationship with a slope coefficient of $k/FTU \approx 0.2$ [77]. Therefore, our FTU estimation corresponds to a k value between 0.2 and 0.3 m^{-1}, which confirms the fitting results. We also note that experimental evidence was reported about a relationship between the light penetration in water and its turbidity, indicating that typical harbor water has $k \sim 0.3\ m^{-1}$ [78]. These values are all related to a single measurement event. It must be stressed that, even in the same location and after few hours, we can realistically expect high fluctuations, with quite worse (or better) k values (see Fig. 5.20).

5.5.2 Experimental setup

The setup used during the experiments is sketched in Fig. 5.21. The modems were clamped to the two posts. Both modems were submerged so that the optical layers (at the top of each) were at 1 m depth. A picture of the modems before submersion is shown in Fig. 5.18c. One of the modems was fastened to a pole and connected via a 25 m long Ethernet cable to a PC. This submarine cable transmits the TCP/IP commands (via power line communication) from the user interface but also supplies 24 V to the modem. The monitoring equipment and the PCs were inside a container on the pier. The second modem acted as a mobile node; thus, it could be moved by a forklift at increasing distances from the first. The second device was also connected to a PC via a similar cable. Since the complete modems

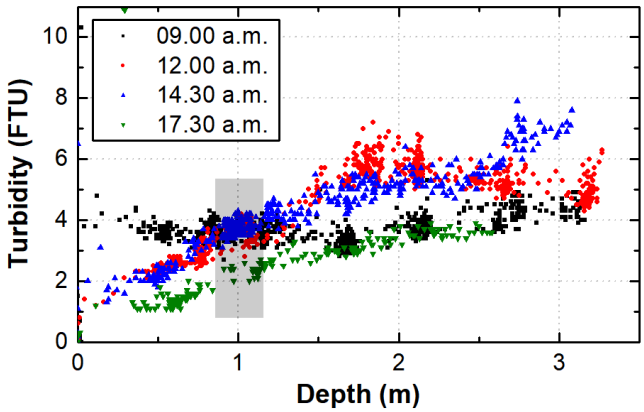

Figure 5.20: Measured turbidity values as a function of depth at different hours in the same day. Note the fluctuation of turbidity within the day but also within the same instrumentation cast.

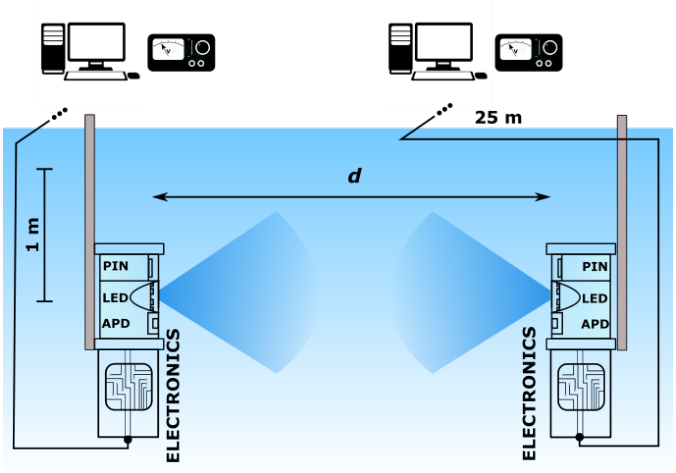

Figure 5.21: Experimental setup of the at-sea tests.

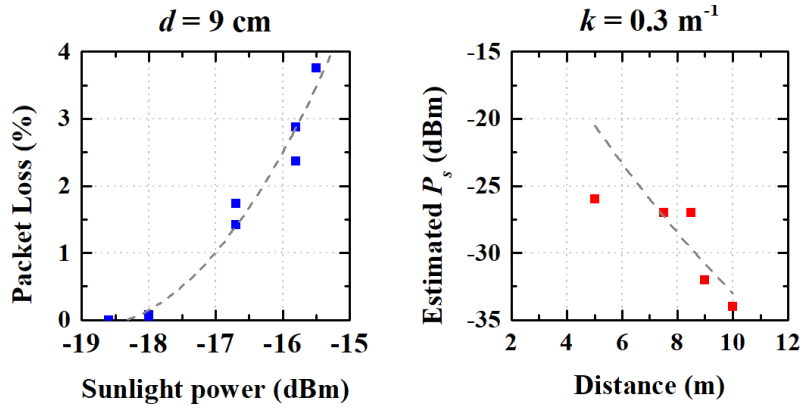

Figure 5.22: Left: observed packet loss as function of the sunlight background illumination, at 9 m distance. Right: summary of estimated signal power as a function of distance, fitted with the attenuation profile assuming $k = 0.3\ m^{-1}$.

were designed to operate with Ethernet 10Base-T, we had no access to their physical layer (e.g., we could not measure eye diagrams, BER etc.). We had only accessible the Ethernet interface through a cable, which could be monitored by sending and receiving Ethernet packets from the PCs, thus measuring the packet loss.

5.5.3 Fixed modems test

During the days of the trials, we faced variable ambient conditions, both in water turbidity and in background light, which both had to be continuously monitored. Particularly, turbidity was unusually high, and this had a strong impact on the signal attenuation.
The communication experiments consisted in repeated file transfers from one PC to the other through the underwater link. In these tests we first measured the packet loss as a function of the distance between the modems (from 2.5 to 10 m), with the modems submerged and fixed on the two poles that were shown in Fig. 5.18c. In order to simulate a real scenario we transferred two different file types as test, i.e., a photo and a video, having size of 3.4 $Mbytes$ and 14.4 $Mbytes$, respectively.

Our measurements started at the shortest distance of 2.5 m: here, not surprisingly, we obtained the best transmission conditions, although we had $P_{BG} \sim P_{RX}$ even with high turbidity and sunlight effect was indeed around $-11.5\ dBm$. Notwithstanding that, the packet loss was always found to be

Packet Sent	P_{BG}(dBm)	Packets Lost	P. Loss (%)
3048	-19.6	14	0.1
3048	-19.6	35	0.2
3048	-19.6	19	0.13
14376	-19.6	9	0.06
14376	-20.4	5	0.03
14376	-20.4	1	0.01
14376	-21.0	0	0
14376	-21.0	0	0

Table 5.2: Packet transmission results at 10 m distance.

d (m)	P_{BG}(dBm)	P_{RX}(dBm)	Turbid. (FTU)	P. Loss (%)
2.5	-11.5	-11.5	$3-4$	0
5.0	-10.4	-22.4	$3-4$	0
7.5	-10.0	-27.0	$3-4$	0.26
10	-21.0	-34.0	$2-3$	0

Table 5.3: Measured parameters and Packet Loss at different distances.

zero. The following measurements were taken at 5 m distance. Here the received signal was lower ($P_{RX} \sim -22\ dBm$) and now the ambient light was higher than the signal. Still the observed packet-loss was zero, in all cases. Further increasing the distance to 7.5 m, made the signal more than 10 times lower than the background at the RX, which gave a minimum ($< 1\%$) loss of data at 7.5 m. Increasing the distance beyond this value, the optical power monitor layer was not able to measure precisely the optical signal power, being too attenuated by the distance. Beyond this distance, we estimated the received optical power exploiting the values collected at shorter distance, adapting the data to distance and turbidity level by using Eq. (5.2.1) (see Section 5.5.3 right). Finally, we transmitted the Ethernet signal over the 10 m distance, which is the maximum expected distance of the OptoCOMM project. At this distance the received optical power was estimated to be around $-34\ dBm$. We transferred several photos and video files in error-free condition, but this was possible only when the background optical power was $-21\ dBm$, at sunset. The measured value of turbidity in this last test fluctuated between $2-3\ FTU$. The results are reported in Table 5.2, where P_{BG} is the optical power of the background light estimated with the PIN PDs. A complete summary of the measured packet loss values taken at different distances is presented in Table 5.3.

Figure 5.23: The UOWC modem equipped under the ROV for mobile transmission.

5.5.4 Mobile transmission test

One of the optical modems was also installed on a small Remotely Operated Vehicle (ROV) (VideoRay Pro4) to test transmission with a moving modem. Fig. 5.23 shows the optical modem clamped under the ROV, which was remotely operated from the pier with a console via umbilical cable. The ROV was exclusively steered in manual mode, without resorting to the vehicle heading and depth control. Fig. 5.24 presents a picture of the experiment. File transmission from the ROV to the fixed node at a maximum range of 5 m was performed, in which the file transferred was the 3.5 $MBytes$ image. The communication was successfully completed: the file was repeatedly transferred in its integrity and the acknowledgment packet was received, over a total transmission time of 10 minutes. The communication quality was not affected, thanks to the chosen beam divergence, not withstanding the ROV that was always in movement during the transmission since the vehicle was manually maneuvered to keep line of sight between the modems. This accomplishment proves also the robustness of the optical modems and the feasibility of optical communication during an operation at sea.

5.5.5 SUNRISE framework integration

Finally, the modems were tested in the fixed configuration when integrated in the SUNSET software framework. The integration was the final goal of our project and it soundly demonstrated that the modems, in their present

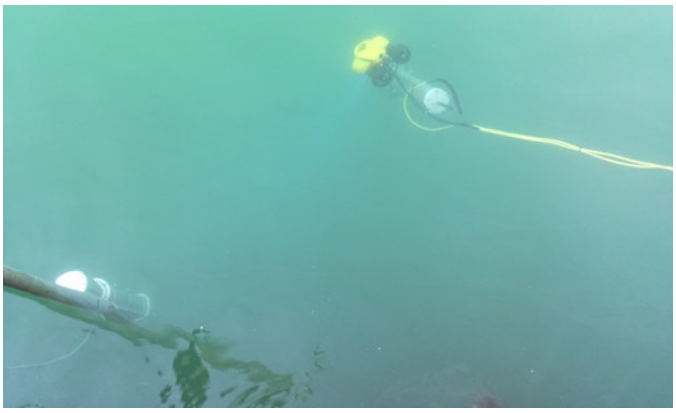

Figure 5.24: Picture of the experiment with a moving UOWC modem installed under the ROV. Both modems are at 1 m depth. Faint blue lights from the modems can be seen, although they suffer from the high turbidity.

form, are already suitable to deploy an Internet of Underwater Things. We note that the modems had been previously tested in the laboratory tests with SUNSET SDCS interface; the same test was repeated during the sea trial. The modems were connected via cables to two instances of SUNSET SDCS running on two different PCs. A Virtual Private Network (VPN) connection between the University of Rome and the harbor of La Spezia allowed the users to access to SUNSET SDCS, whose fragmentation module was used to transmit large files overcoming the constraints of the maximum packet size of the optical modem. Several files with different sizes, ranging from 11 $MBytes$ to 1.5 $GBytes$, were optically transmitted. The maximum payload size for each packet was 5 $Mbytes$; the greater files were fragmented by the SUNSET SDCS fragmentation module at the TX and then reassembled by the RX. Fig. 5.25 illustrates the setup during the experiments. All files were successfully transmitted between the optical modems and sent back to another SUNSET remote station. The test was performed with the modems at a distance of 5 m, with background optical power (due to sunlight illumination) of approximately -11 dBm (average through the experimental time). It is worth noting that, while the optical modems operated always at 10 $Mbit/s$ rate, the overall SUNSET network rate was on average 4 $Mbit/s$ (see Table 5.4), mainly due to delay and latency introduced by the VPN. The results were very similar to what had been previously achieved within the lab testing. This confirmed the achievement of the integration between the optical modems and the SUNSET framework also in at sea operative

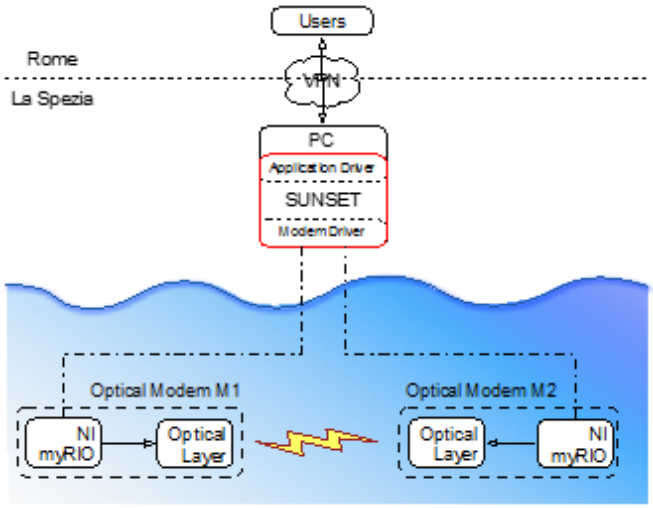

Figure 5.25: Block-diagram of the remote connection through the SUNSET framework

scenarios.

File size (MB)	Chunks	Bit Rate (Mbit/s)	P. Loss (%)
11	3	4.70	0
46	10	4.15	0
106	22	4.27	0
354	72	3.99	0
500	101	4.30	0
750	151	4.27	0
1250	251	4.31	0
1500	301	4.26	0

Table 5.4: Packet transmission results in SUNSET integration.

Chapter 6

Conclusions

In this thesis we presented the development of three systems for a practical implementation of VLC technology in real scenarios, relying on existing infrastructures with limited or no reconfiguration required.
In Chapter 3 we have presented the upgrade of a common commercial lamp to a ND-LOS VLC system, transmitting 10Base-T Ethernet signals. The system achieved a BER of 10^{-9}, even in highly illuminated environments, with moderate signal light intensity ($\sim 50\ lux$). The proposed VLC system showed a strong tolerance to misalignment up ± 45 degrees and provided a transmission fully compatible with the Ethernet standard over a $> 90\ cm$ radius circular area over a common desktop surface. To the best of our knowledge, this system was the first successful integration of commercial lighting equipment and VLC data transmission by a very limited in-line additive hardware upgrade.
Our implementation did not require any special component, nor any complex modulation format.
The lamp prototype took part as demonstrator in the Artemide S.p.A. company showroom at "Light and Building 2016" international exposition in Frankfurt.
In Chapter 4 we showed the use of RoI detection to enhance the performance of a RS-OCC system. We used the RoI detection scheme to estimate and measure the impact of the transmission span in RS-OCC systems, proposing a RoI-assisted DSP to recover the signal distortion induced by the shape of light sources used as VLC transmitters. The proposed solution demonstrated to remove the distortion up to a link span of 1 m, doubling the distance obtained by previous results of other distortion removing systems. RS-OCC channels are intrinsically bursty, especially with increasing link

span. In the absence of synchronization we proposed a suitable solution to avoid data loss by simulating the use of two repeated packet transmission schemes. The results of the simulations showed promising results that could be applied in unidirectional transmission for mass deployed OCC systems.
In Chapter 5 we presented the design and field demonstration of a novel UOWC system, useful for practical marine applications and fully compatible with 10Base-T Ethernet transmission (10 $Mbit/s$ with a Manchester-coded signal). The modems included a LED-based photonic section, an electronic part and a software part for integration within the SUNRISE European project networking architecture.
The complete final version of the modems was tested at sea, in harbor condition (high turbidity) and with sunlight disturbance. During the tests, the measured turbidity level at the transmission depth was between 2.5 and 5 FTU. Performance in the final test was assessed by measuring the packet loss as a function of distance, while monitoring water turbidity and background optical power. The system was proven error-free or with negligible packet loss up to a range of 7.5 m in full daylight and very high turbidity. At sunset, with decrease of the optical noise to -21 dBm, the system achieved error-free transmission at 10 m. In both cases (full daylight, sunset) the performance achieved was better than any other reported systems in comparable conditions.
We also successfully carried out a transmission between a fixed and a mobile node with one of the modems installed on a ROV. This accomplishment assessed the good robustness of the adopted technology, based on diverging beams, and the feasibility in the employment of such technology in at sea operative scenarios.
Finally, we successfully tested the integration between the SUNSET SDCS and the optical modems during the experiment to guarantee interfacing and networking possibilities.
While all the tests reported are indeed in harbor, the design requirements are not restricted to shallow water. Therefore, our developed modems reached the right trade-off that could guarantee improved performance (w.r.t. the state-of-the-art) in shallow waters without degrading the expected performance in deep, dark and clear waters.
While open sea, deep-water transmission was not tested, the laboratory calibrations and the estimated relation between turbidity and extinction coefficient allow to predict an achievable transmission range of at least 40 m in deep, dark waters. The general conclusion is that VLC are an attractive solution to complement RF wireless technology in many areas. We have demonstrated that VLC system represent a mature realization that can be

deployed in real in-field application in different areas and integrated in the existing network architectures. The results of this thesis demonstrated a range of new possibilities enabled by VLC to be developed in the near future: ultra dense mobile communications exploiting a network embedded within the lighting infrastructure; secure PAN that cannot be eavesdropped or jammed; PD-less optical systems, ubiquitously deployed using personal smartphones and security cameras; AUV coordinated swarms for seabed monitoring or scouting for new resources at the bottom of the oceans, like oil or rare earths; and many more.

Bibliography

[1] F. R. Gfeller and U. Bapst, "Wireless In-House Data Communication via Diffuse Infrared Radiation," *Proceedings of the IEEE*, vol. 67, no. 11, pp. 1474–1486, 1979. [Online]. Available: http://ieeexplore.ieee.org/document/1455777/

[2] "VLCA Visible Light Communications Association Website." [Online]. Available: http://vlca.net/

[3] "Clean Energy Ministerial —Global Lighting Challenge — Advancing Clean Energy Together." [Online]. Available: http://www.cleanenergyministerial.org/campaign-clean-energy-ministerial/global-lighting-challenge

[4] "Light Communications for Wireless Local Area Networking - IEEE Future Networks." [Online]. Available: https://futurenetworks.ieee.org/tech-focus/may-2018/light-communications-for-wireless-local-area-networking

[5] "UNITED STATES THE RADIO SPECTRUM." [Online]. Available: https://www.ntia.doc.gov/files/ntia/publications/2003-allochrt.pdf

[6] G. P. Agrawal, *Fiber-optic communication systems*. Wiley, 2013.

[7] "Cisco Visual Networking Index: Forecast and Trends, 2017–2022," Tech. Rep., 2018. [Online]. Available: https://www.cisco.com/c/en/us/solutions/collateral/service-provider/visual-networking-index-vni/white-paper-c11-741490.pdf

[8] M. Botterman, "For the European Commission Information Society and Media Directorate General," in *Networked Enterprise & RFID Unit–D4, Internet of Things: An Early Reality of the Future Internet, Report of the Internet of Things Workshop, Prague, Czech Republic*, 2009.

[9] Nokia Bell Labs, "Mobility Traffic Report," Tech. Rep., 2016.

[10] "Cooper's Law — ArrayComm." [Online]. Available: http://www.arraycomm.com/technology/coopers-law/

[11] O. S. Board and N. R. Council, *Exploration of the Seas: Voyage into the Unknown*. National Academies Press, 2003.

[12] H. Kaushal and G. Kaddoum, "Underwater Optical Wireless Communication," *IEEE Access*, vol. 4, pp. 1518–1547, 2016. [Online]. Available: http://ieeexplore.ieee.org/document/7450595/

[13] W. Huang, P. Tian, and Z. Xu, "Design and implementation of a real-time CIM-MIMO optical camera communication system," *Optics Express*, vol. 24, no. 21, p. 24567, 10 2016. [Online]. Available: https://www.osapublishing.org/abstract.cfm?URI=oe-24-21-24567

[14] Y. Goto, I. Takai, T. Yamazato, H. Okada, T. Fujii, S. Kawahito, S. Arai, T. Yendo, and K. Kamakura, "A New Automotive VLC System Using Optical Communication Image Sensor," *IEEE Photonics Journal*, vol. 8, no. 3, pp. 1–17, 6 2016. [Online]. Available: http://ieeexplore.ieee.org/document/7454688/

[15] Z. Ghassemlooy, S. Arnon, M. Uysal, Z. Xu, and J. Cheng, "Emerging Optical Wireless Communications-Advances and Challenges," *IEEE Journal on Selected Areas in Communications*, vol. 33, no. 9, pp. 1738–1749, 9 2015.

[16] T. Q. Khan, P. Bodrogi, Q. T. Vinh, and H. Winkler, *LED Lighting : Technology and Perception.* Wiley, 2014.

[17] G. P. G. P. Agrawal, *Lightwave technology : components and devices*. John Wiley, 2004.

[18] S. Arnon, *Visible light communication*.

[19] J. R. Barry, *Wireless Infrared Communications*. Boston, MA: Springer US, 1994.

[20] G. E. Thomas and K. Stamnes, *Radiative transfer in the atmosphere and ocean*. Cambridge University Press, 2002.

[21] A. J. Moreira, R. T. Valadas, and A. de Oliveira Duarte, "Optical interference produced by artificial light," *Wireless Networks*,

vol. 3, no. 2, pp. 131–140, 1997. [Online]. Available: http://link.springer.com/10.1023/A:1019140814049

[22] R. Seifert and Rich, *Gigabit Ethernet : technology and applications for high speed LANs*. Addison-Wesley, 1998. [Online]. Available: https://dl.acm.org/citation.cfm?id=522012

[23] N. Chi, Y. Zhou, J. Shi, Y. Wang, and X. Huang, "Enabling Technologies for High Speed Visible Light Communication," in *Optical Fiber Communication Conference*. Washington, D.C.: OSA, 3 2017, p. Th1E.3. [Online]. Available: https://www.osapublishing.org/abstract.cfm?URI=OFC-2017-Th1E.3

[24] S. Pergoloni, M. Biagi, S. Rinauro, S. Colonnese, R. Cusani, and G. Scarano, "Merging Color Shift Keying and Complementary Pulse Position Modulation for Visible Light Illumination and Communication," *Journal of Lightwave Technology*, vol. 33, no. 1, pp. 192–200, 1 2015. [Online]. Available: http://ieeexplore.ieee.org/document/6998813/

[25] M. Biagi, A. M. Vegni, S. Pergoloni, P. M. Butala, and T. D. C. Little, "Trace-Orthogonal PPM-Space Time Block Coding Under Rate Constraints for Visible Light Communication," *Journal of Lightwave Technology*, vol. 33, no. 2, pp. 481–494, 1 2015. [Online]. Available: http://ieeexplore.ieee.org/document/7000619/

[26] G. Cossu, A. M. Khalid, R. Corsini, and E. Ciaramella, "Non-Directed Line-of-Sight Visible Light System providing High-Speed and Robustness to Ambient Light," in *Optical Fiber Communication Conference/National Fiber Optic Engineers Conference 2013*. Washington, D.C.: OSA, 2013, p. OTh1G.2. [Online]. Available: https://www.osapublishing.org/abstract.cfm?uri=OFC-2013-OTh1G.2

[27] G. Cossu, R. Corsini, and E. Ciaramella, "High-Speed Bi-directional Optical Wireless System in Non-Directed Line-of-Sight Configuration," *Journal of Lightwave Technology*, vol. 32, no. 10, pp. 2035–2040, 5 2014. [Online]. Available: https://www.osapublishing.org/jlt/abstract.cfm?uri=jlt-32-10-2035

[28] G. Cossu, R. Corsini, A. M. Khalid, and E. Ciaramella, "Bi-directional 400 Mbit/s LED-based optical wireless communication for non-directed line-of-sight transmission," in *Optical Fiber Communications Conference and Exhibition (OFC), 2014*. IEEE, pp. 1–3.

[29] P. Brandl, R. Enne, T. Jukic, and H. Zimmermann, "OWC Using a Fully Integrated Optical Receiver With Large-Diameter APD," *IEEE Photonics Technology Letters*, vol. 27, no. 5, pp. 482–485, 3 2015. [Online]. Available: http://ieeexplore.ieee.org/document/6994819/

[30] C. Chen, R. Bian, and H. Haas, "Omnidirectional Transmitter and Receiver Design for Wireless Infrared Uplink Transmission in LiFi," in *2018 IEEE International Conference on Communications Workshops (ICC Workshops)*. IEEE, 5 2018, pp. 1–6. [Online]. Available: https://ieeexplore.ieee.org/document/8403727/

[31] Comité Europeén de Normalisation, "European Standard EN 12464-1: Lighting of Workplaces: Indoor workplaces," *Brussels: CEN*, 2003.

[32] N. Kumar and N. R. Lourenco, "Led-based visible light communication system: a brief survey and investigation," *J. Eng. Appl. Sci*, vol. 5, no. 4, pp. 296–307, 2010.

[33] T. Komine and M. Nakagawa, "Fundamental analysis for visible-light communication system using LED lights," *IEEE transactions on Consumer Electronics*, vol. 50, no. 1, pp. 100–107, 2004.

[34] N. T. Le, M. S. Ifthekhar, Y. M. Jang, and N. Saha, "Survey on optical camera communications: challenges and opportunities," *IET Optoelectronics*, vol. 9, no. 5, pp. 172–183, 10 2015. [Online]. Available: https://digital-library.theiet.org/content/journals/10.1049/iet-opt.2014.0151

[35] "Sony Xperia XZ Premium Full Specifications." [Online]. Available: https://www.sonymobile.com/gb/products/phones/xperia-xz-premium/specifications/

[36] "Phantom v711 Full Specifications." [Online]. Available: https://www.phantomhighspeed.com/products/cameras/vseries/v711

[37] C. Danakis, M. Afgani, G. Povey, I. Underwood, and H. Haas, "Using a CMOS camera sensor for visible light communication," in *2012 IEEE Globecom Workshops*. IEEE, 12 2012, pp. 1244–1248. [Online]. Available: http://ieeexplore.ieee.org/document/6477759/

[38] W.-C. Wang, C.-W. Chow, C.-W. Chen, H.-C. Hsieh, and Y.-T. Chen, "Beacon Jointed Packet Reconstruction Scheme for Mobile-Phone Based Visible Light Communications Using Rolling Shutter," *IEEE*

Photonics Journal, vol. 9, no. 6, pp. 1–6, 12 2017. [Online]. Available: http://ieeexplore.ieee.org/document/8068179/

[39] W. Hu, H. Gu, and Q. Pu, "LightSync: Unsynchronized visual communication over screen-camera links," in *Proceedings of the 19th annual international conference on Mobile computing & networking - MobiCom '13*. New York, New York, USA: ACM Press, 2013, p. 15. [Online]. Available: http://dl.acm.org/citation.cfm?doid=2500423.2500437

[40] J.-W. Lee, S.-H. Yang, and S.-K. Han, "Optical Pulse Width Modulated Multilevel Transmission in CIS-Based VLC," *IEEE Photonics Technology Letters*, vol. 29, no. 15, pp. 1257–1260, 8 2017. [Online]. Available: http://ieeexplore.ieee.org/document/7953536/

[41] Y.-S. Kuo, P. Pannuto, K.-J. Hsiao, and P. Dutta, "Luxapose: Indoor Positioning with Mobile Phones and Visible Light," in *Proceedings of the 20th annual international conference on Mobile computing and networking - MobiCom '14*. ACM, 2014, pp. 447–458. [Online]. Available: http://dx.doi.org/10.1145/2639108.2639109http://dl.acm.org/citation.cfm?doid=2639108.2639109

[42] D. Litwiller, "Ccd vs. cmos," *Photonics Spectra*, vol. 35, no. 1, pp. 154–158, 2001.

[43] "[Product Brief] IMX230 Diagonal 7.487 mm (Type 1/2.4) 21Mega-Pixel CMOS Image Sensor with Square Pixel for Color Cameras," Tech. Rep. [Online]. Available: https://www.sony-semicon.co.jp/products_en/IS/sensor1/img/products/ProductBrief_IMX230_20150427.pdf

[44] N. Otsu, "A threshold selection method from gray-level histograms," *IEEE transactions on systems, man, and cybernetics*, vol. 9, no. 1, pp. 62–66, 1979.

[45] J. Kittler and J. Illingworth, "On threshold selection using clustering criteria," *IEEE transactions on systems, man, and cybernetics*, no. 5, pp. 652–655, 1985.

[46] K. Alam, T. Ray, and S. G. Anavatti, "A brief taxonomy of autonomous underwater vehicle design literature," *Ocean Engineering*, vol. 88, pp. 627–630, 2014.

[47] S.-K. Jeong, H.-S. Choi, J.-H. Bae, S.-S. You, H. S. Kang, S.-J. Lee, J.-Y. Kim, D.-H. Kim, and Y.-K. Lee, "Design and control of high speed unmanned underwater glider," *International Journal of Precision Engineering and Manufacturing-Green Technology*, vol. 3, no. 3, pp. 273–279, 2016. [Online]. Available: http://dx.doi.org/10.1007/s40684-016-0035-1

[48] T. Battista, C. Woolsey, T. Perez, and F. Valentinis, "A Dynamic Model for Underwater Vehicle Maneuvering Near a Free Surface," *IFAC-PapersOnLine*, vol. 49, no. 23, pp. 68–73, 2016.

[49] M. Kojima, A. Asada, K. Mizuno, K. Nagahashi, F. Katase, Y. Saito, and T. Ura, "AUV IRSAS for submarine hydrothermal deposits exploration," in *2016 IEEE/OES Autonomous Underwater Vehicles (AUV)*, pp. 161–164.

[50] S. D. Ling, I. Mahon, M. P. Marzloff, O. Pizarro, C. R. Johnson, and S. B. Williams, "Stereo-imaging AUV detects trends in sea urchin abundance on deep overgrazed reefs," *Limnology and Oceanography: Methods*, vol. 14, no. 5, pp. 293–304, 5 2016. [Online]. Available: http://doi.wiley.com/10.1002/lom3.10089

[51] S. Sendra, J. V. Lamparero, J. Lloret, and M. Ardid, "Study of the optimum frequency at 2.4 GHz ISM band for underwater wireless ad hoc communications," in *International Conference on Ad-Hoc Networks and Wireless*. Springer, pp. 260–273.

[52] S. I. Inacio, M. R. Pereira, H. M. Santos, L. M. Pessoa, F. B. Teixeira, M. J. Lopes, O. Aboderin, and H. M. Salgado, "Dipole antenna for underwater radio communications," in *3rd Underwater Communications and Networking Conference, Ucomms 2016*. IEEE, 8 2016, pp. 1–5. [Online]. Available: http://ieeexplore.ieee.org/document/7583457/

[53] E. Jimenez, G. Quintana, P. Mena, P. Dorta, I. Perez-Alvarez, S. Zazo, M. Perez, and E. Quevedo, "Investigation on radio wave propagation in shallow seawater: Simulations and measurements," in *Underwater Communications and Networking Conference (UComms), 2016 IEEE Third*. IEEE, pp. 1–5.

[54] U. M. Qureshi, F. K. Shaikh, Z. Aziz, S. M. Z. S. Shah, A. A. Sheikh, E. Felemban, and S. B. Qaisar, "RF Path and Absorption Loss Esti-

mation for Underwater Wireless Sensor Networks in Different Water Environments," *Sensors*, vol. 16, no. 6, p. 890, 2016.

[55] J.-H. Cui, J. Kong, M. Gerla, and S. Zhou, "The challenges of building mobile underwater wireless networks for aquatic applications," *Ieee Network*, vol. 20, no. 3, pp. 12–18, 2006.

[56] D. E. Chaitanya, C. V. Sridevi, and G. S. B. Rao, "Path loss analysis of underwater communication systems," in *Students' Technology Symposium (TechSym), 2011 IEEE*. IEEE, pp. 65–70.

[57] B. Li, J. Huang, S. Zhou, K. Ball, M. Stojanovic, L. Freitag, and P. Willett, "Further results on high-rate MIMO-OFDM underwater acoustic communications," in *OCEANS 2008*. IEEE, pp. 1–6.

[58] H. Kaushal and G. Kaddoum, "Underwater Optical Wireless Communication," *IEEE Access*, vol. 4, pp. 1518–1547, 2016.

[59] K. Nakamura, I. Mizukoshi, and M. Hanawa, "Optical wireless transmission of 405 nm, 1.45 Gbit/s optical IM/DD-OFDM signals through a 4.8 m underwater channel," *Optics express*, vol. 23, no. 2, pp. 1558–1566, 2015.

[60] H. M. Oubei, J. R. Duran, B. Janjua, H.-Y. Wang, C.-T. Tsai, Y.-C. Chi, T. K. Ng, H.-C. Kuo, J.-H. He, and M.-S. Alouini, "4.8 Gbit/s 16-QAM-OFDM transmission based on compact 450-nm laser for underwater wireless optical communication," *Optics express*, vol. 23, no. 18, pp. 23 302–23 309, 2015.

[61] J. Xu, M. Kong, A. Lin, Y. Song, X. Yu, F. Qu, J. Han, and N. Deng, "OFDM-based broadband underwater wireless optical communication system using a compact blue LED," *Optics Communications*, vol. 369, pp. 100–105, 2016.

[62] J. W. Giles and I. N. Bankman, "Underwater optical communications systems. Part 2: basic design considerations," in *MILCOM 2005-2005 IEEE Military Communications Conference*. IEEE, pp. 1700–1705.

[63] A. Boucouvalas, K. Peppas, K. Yiannopoulos, and Z. Ghassemlooy, "Underwater Optical Wireless Communications with Optical Amplification and Spatial Diversity," *IEEE Photonics Technology Letters*, 2016.

[64] B. M. Cochenour, L. J. Mullen, and A. E. Laux, "Characterization of the beam-spread function for underwater wireless optical communications links," *IEEE Journal of Oceanic Engineering*, vol. 33, no. 4, pp. 513–521, 2008.

[65] H. Zhang and Y. Dong, "Impulse response modeling for general underwater wireless optical MIMO links," *IEEE Communications Magazine*, vol. 54, no. 2, pp. 56–61, 2016.

[66] S. Reed, J. Wood, and C. Haworth, "The detection and disposal of IED devices within harbor regions using AUVs, smart ROVs and data processing/fusion technology," in *2010 International Waterside Security Conference, WSS 2010*. IEEE, 11 2010, pp. 1–7. [Online]. Available: http://ieeexplore.ieee.org/document/5730276/

[67] G. Cossu, R. Corsini, A. M. Khalid, S. Balestrino, A. Coppelli, A. Caiti, and E. Ciaramella, "Experimental demonstration of high speed underwater visible light communications," in *2nd International Workshop on Optical Wireless Communications (IWOW)*. IEEE, pp. 11–15.

[68] "SUNRISE." [Online]. Available: http://www.fp7-sunrise.eu/

[69] A. Caiti, E. Ciaramella, G. Conte, G. Cossu, D. Costa, S. Grechi, R. Nuti, D. Scaradozzi, and A. Sturniolo, "OptoCOMM : introducing a new optical underwater wireless communication modem," *2016 IEEE Third Underwater Communications and Networking Conference (UComms)*, pp. 2–6, 8 2016. [Online]. Available: http://ieeexplore.ieee.org/document/7583431/

[70] A. Bartolini, A. Caiti, E. Ciaramella, G. Conte, G. Cossu, D. Costa, S. Grechi, R. Nuti, D. Scaradozzi, and A. Sturniolo, "OptoCOMM: Development and experimentation of a new optical wireless underwater modem," in *OCEANS 2016 MTS/IEEE Monterey*. IEEE, pp. 1–5.

[71] G. Cossu, A. Sturniolo, A. Messa, D. Scaradozzi, and E. Ciaramella, "Full-Fledged 10Base-T Ethernet Underwater Optical Wireless Communication System," pp. 1–1, 2017. [Online]. Available: http://ieeexplore.ieee.org/document/8113454/

[72] G. Cossu, A. Sturniolo, A. Messa, S. Grechi, D. Scaradozzi, A. Caiti, and E. Ciaramella, "Sea-trial of an Ethernet-based Underwater VLC Communication System," in *2018 Optical Fiber Communications Conference and Exposition (OFC)*. IEEE, 2018, pp. 1–3.

[73] G. Cossu, A. Sturniolo, A. Messa, S. Grechi, D. Costa, A. Bartolini, D. Scaradozzi, A. Caiti, and E. Ciaramella, "Sea-Trial of Optical Ethernet Modems for Underwater Wireless Communications," *Journal of Lightwave Technology*, vol. 36, no. 23, pp. 5371–5380, 12 2018. [Online]. Available: https://ieeexplore.ieee.org/document/8468031/

[74] D. J. Segelstein, "The complex refractive index of water," Ph.D. dissertation, 1981.

[75] *IEEE Std 802.3-2015 (Revision of IEEE Std 802.3-2012) : IEEE Standard for Ethernet.* IEEE, 2016. [Online]. Available: https://ieeexplore.ieee.org/document/7428776/figures#figures

[76] A. Caiti, P. Gjanci, S. Grechi, R. Nuti, C. Petrioli, L. Picari, and D. Spaccini, "OptoCOMM and SUNSET to enable large data offloading in Underwater Wireless Sensor Networks," in *OCEANS 2016 MTS/IEEE Monterey*. IEEE, 9 2016, pp. 1–5. [Online]. Available: http://ieeexplore.ieee.org/document/7761226/

[77] L. Ulrik and K. Bundgaard, "Studies of the relationship between suspended sediment concentration and light attenuation," in *BOOK OF ABSTRACTS*.

[78] W. A. Swenson, *Influence of turbidity on fish abundance in western Lake Superior*. Environmental Protection Agency, Office of Research and Development, Environmental Research Laboratory, 1978.

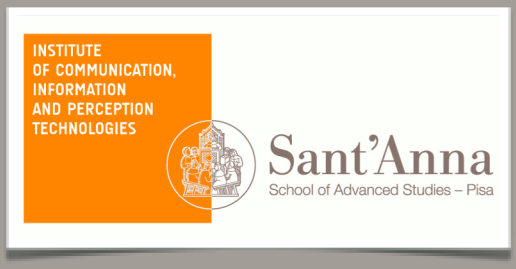
INSTITUTE
OF COMMUNICATION,
INFORMATION
AND PERCEPTION
TECHNOLOGIES
Sant'Anna
School of Advanced Studies – Pisa